Bioelectronic cell-based device provides a strategy for the treatment of the experimental model of multiple sclerosis

Emilie Audouard, Fanny Michel, Vanessa Pierroz, Taeuk Kim, Lisa Rousselot, Béatrix Gillet-Legrand, Gaëlle Dufayet-Chauffaut, Peter Buchmann, Michael Florea, Alexander Khel, et al.

Journal of Controlled Release 352 (2022) 994–1008

Contents lists available at ScienceDirect

Journal of Controlled Release

journal homepage: www.elsevier.com/locate/jconrel

Bioelectronic cell-based device provides a strategy for the treatment of the experimental model of multiple sclerosis

Emilie Audouard [a,1], Fanny Michel [b,1], Vanessa Pierroz [b], Taeuk Kim [b], Lisa Rousselot [a], Béatrix Gillet-Legrand [a], Gaëlle Dufayet-Chauffaut [a], Peter Buchmann [b], Michael Florea [b], Alexander Khel [c], Kamilya Altynbekova [c], Claudia Delgaldo [d], Encarna Escudero [d], Alejandra Ben Aissa Soler [d], Nathalie Cartier [a], Francoise Piguet [a,1], Marc Folcher [b,e,*,1,2]

[a] NeuroGenCell, Paris Brain Institute – ICM, INSERM, CNRS, AP-HP, Sorbonne Université; Hôpital de la Pitié Salpètrière, Paris, France
[b] Department of Biosystems Science and Engineering, D-BSSE, ETH Zürich, Basel, Switzerland
[c] GeneXplain GmbH, Wolfenbuettel, Germany
[d] Eurecat, Centre Tecnològic de Catalunya, Functional Printing and Embedded Devices Unit, Mataró, Spain
[e] Institute of Molecular and Clinical Ophthalmology, IOB, Basel, Switzerland

ARTICLE INFO

Keywords:
Cell-based device
Optogenetic
Bioelectronic
Drug delivery
Multiple sclerosis
Interferon

ABSTRACT

Wireless powered optogenetic cell-based implant provides a strategy to deliver subcutaneously therapeutic proteins. Immortalize Human Mesenchymal Stem Cells (hMSC-TERT) expressing the bacteriophytochrome diguanylate cyclase (DGCL) were validated for optogenetic controlled interferon-β delivery (Optoferon cells) in a bioelectronic cell-based implant. Optoferon cells transcriptomic profiling was used to elaborate an in-silico model of the recombinant interferon-β production. Wireless optoelectronic device integration was developed using additive manufacturing and injection molding. Implant cell-based optoelectronic interface manufacturing was established to integrate industrial flexible compact low-resistance screen-printed Near Field Communication (NFC) coil antenna. Optogenetic cell-based implant biocompatibility, and device performances were evaluated in the Experimental Autoimmune Encephalomyelitis (EAE) mouse model of multiple sclerosis.

1. Introduction

Advance Therapeutic Medicinal Products (ATMP) hold the promise to treat many diseases with a high-unmet medical need. Most ATMP's in development target autoimmune disease, neurodegenerative disease, and previously untreated disease [1]. Synthetic biology tools have offered numerous possibilities to program theragnostic prosthetic gene networks into mammalian "smart" cells [2]. Elegant proofs of concept demonstrated the therapeutic potential of cell-based implants to offer an alternative strategy to treat diabetes [3–5], hormonal imbalance [6], and metabolic diseases [7]. Far-red to near-infrared (NIR) wavelength actuated enzyme photoreceptors bear unique property to develop optogenetic interfaces between implanted electronic and living systems [8,9]. Synthetic optogenetic pathways integrating engineered bacteriophytochrome-associated diguanylate cyclases (DGCL, BphS) operate as a light-triggered transcription switch to control cell protein production capacity [8,10,11] (Fig. 1A). Implantable cell-based devices validated for clinical use act as a confinement barrier to protect the patient from the grafted cells while allowing the diffusion of therapeutic effectors in the blood circulation [5]. Recent developments in bioengineering have paved the way for the translation of retrievable macroencapsulation cell technology to the bedside [1,5,12,13]. Flat-sheet cell-based device requirements define the best environment to support the growth of the therapeutic cells while providing immune isolation [12,13]. 3D printing technology has opened a new avenue to manufacture custom design medical devices and implantable cell-based devices [14–16]. Wireless powered bioelectronic cell-based implant combines a confinement cell chamber module with a wireless powered optoelectronic interface [10,17]. The optoelectronic integrating cell-based device technology opens the possibility of subcutaneously

* Corresponding author at: Department of Biosystems Science and Engineering, D-BSSE, ETH Zürich, Basel, Switzerland.
E-mail address: Marc.folcher@iob.ch (M. Folcher).
[1] Authors contributed equally
[2] Present address: Institute of Molecular and Clinical Ophthalmology, IOB; Basel, Switzerland

https://doi.org/10.1016/j.jconrel.2022.11.008
Received 12 August 2022; Received in revised form 25 October 2022; Accepted 4 November 2022
Available online 16 November 2022

remote-control drug-delivery with optogenetic programmed encapsulated cells. By coupling a brain-computer interface (BCI) to a wireless powered optogenetic cell-based implant, a proof-of-concept study demonstrated that it was even possible to remote control protein delivery by the mind [10]. Optogenetic programmed cells embedded in a hydrogel with wireless powered NIR LED were implanted to support a cure for the type I diabetes in rodent model [11]. A major roadblock for the clinical development of synthetic biology-derived bioelectronic cell-based therapy is the lack of industrially manufactured cell-therapy delivery vehicles [5,18]. Interferons (IFNs), biopharmaceutical agents were qualified as viral interference in 1957, and remain today the frontlines of antiviral defense mechanism against retrovirus like the coronavirus [19,20]. Their immune-modulatory action is beneficial for the patient suffering from multiple sclerosis [21,22], but their mode of action remains not fully understood. Despite the new therapeutic avenues drawn by immunotherapies, Interferon-beta remains prescribed therapeutic protein which posology needs to be adjusted to the patient's needs [22,23]. While the optogenetic cell-based therapy (Optogenerapy) technology is still in its infancy, pharma economic analysis shows that the technology offers economic advantages available to drug prescription [24]. Essential steps need to be taken to translate the bioelectronic device requirements into an industrial manufactured medical-grade device. In this study, we have set the bases for the industrial manufacturing and bio-manufacturing process to produce bioelectronic implantable devices integrating optogenetic programmed cells delivering interferon. In-depth transcriptional pathway activation analysis of the programmed Optoferon cells was used to model the optogenetic pathway activation in the cells. The therapeutic action of the implantable bioelectronic device was programmed by loading Optoferon cells in the implant cell chamber. The efficacy of the interferon-beta drug-delivery technology was validated using the EAE mice model of multiple sclerosis [25]. Activated implanted devices offered neurodegenerative protection in the EAE mice model of multiple sclerosis.

2. Results

2.1. Synthetic optogenetic pathway engineering

The synthetic optogenetic pathway operating as a light-triggered transcription switch capitalizes on the ubiquitous bacterial second messenger cyclic diguanylate monophosphate (*c*-di-GMP). The optogenetic pathway integrates a bacteriophytochrome that functions as light-activated cyclic diguanylate monophosphate (*c*-di-GMP) synthase [8,10] (Fig. 1A**).** NIR illumination induces the intracellular surge of the ubiquitous bacterial second messenger *c*-di-GMP that binds to the reticulum endoplasmic residing stimulator of interferon gene (STING) to specify phosphorylation of TBK1 and IRF3 [26]. Phosphorylated IRF3 localizes to the nucleus to activate interferon sensitive response elements (ISRE) (Fig. 1A). To test the performance of the system in the different cellular backgrounds, the individual system components were transfected in the presence of a reporter plasmid harboring the human secreted alkaline phosphatase (SEAP) gene driven by an IRF3 optimized human interferon promoter PSO3 ($PIFN_{(ACD+)}$-SEAP-pA) [10,27]. The synthetic optogenetic pathway is composed of the photoactivatable diguanylate cyclase plasmid PKZY113 (PSV40-DGCL-pA); the stimulator of interferon gene STING expression plasmid (pSTING). The system components were co-transfected in a HEK293 FT; CHO; hMSC-MNSOD; and hMSC-TERT cells (Fig. 1B**).** The data confirmed that despite difference in performance the transient expression of the bacteriophytochrome photoactivatable system was functional in the different cellular background (Fig. 1B) [10]. The diversity of response observed in the different cellular background is associated with the STING polymorphism and the different promoter strength conferred by the respective cell lineage. The hMSC-TERT cell created by overexpression of human telomerase reverse transcriptase (hTERT) gene in cultured human skeletal (marrow stromal) stem cells (hMSC). The immortalized hMSC-TERT cell line was preferred because they were characterized and validated for use in cell therapy context [50–51] and show neither toxicity nor tumorigenic properties [28–51]. Also, the choice of a

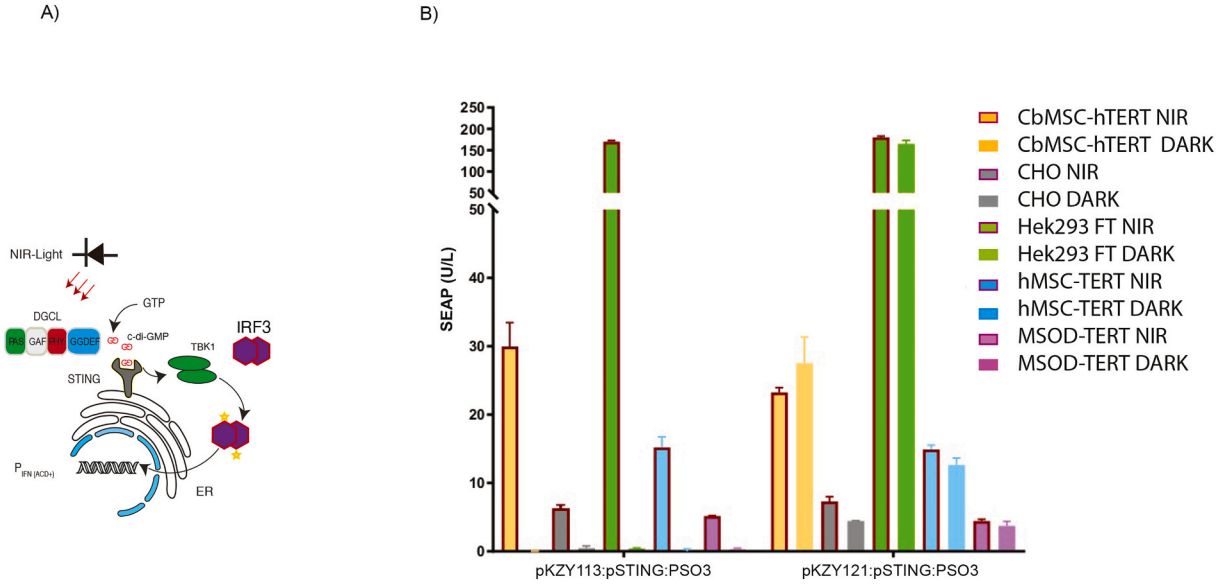

Fig. 1. (A) Optogenetic synthetic pathways. NIR-light triggers the activation of the light activable Diguanylate cyclase (DGCL) to produced *c*-di-GMP. Reticulum endoplasmic residing STING binds *c*-di-GMP and mediate TBK1/IRF3 phosphorylation and subsequent IRF3 nuclear localization to activate an optimized Interferon beta promoter $P_{IFN(ACD+)}$. (B) Vector encoding photoactivable DGCL pKZY113 (P_{SV40}-DGCL-pA) or the constitutive diguanylate cyclase A pKZY121 (P_{SV40}-$DGCA_{CC3285}$-pA) were transfected in the presence of the STING expression plasmid pSTING (P_{hCMV}-STING-pA) and the reporter SEAP pSO3 ($PIFN_{(ACD+)}$-SEAP-pA) in a panel of cell lines. The system performance expressing either the DGCL photoactivable DGC allele (pKZY113) or the constitutively active DGC (pKZY121) were compared among a cell line panel composed of: Immortalized Human Cord Blood Mesenchymal Stromal Cells (cbMSC-hTERT); Chinese hamster ovary K1 (CHO-K1), Human embryonic kidney (HEK) 293 FT cells (CVCL_6911) human bone marrow-derived Mesenchymal Stromal Cells (hMSCs) [50], the HMSC integrating hTERT and inducible Caspase 9 cell line is annotated hMSC-MSOD [51]. Transfected cells were kept in dark (DARK) or exposed to 4 h NIR and the SEAP (U/L) was measured in the medium supernatant after 48 h.

validated immortalized cell line as an engineering template will facilitate the translation of the project to the GMP production and clinic.

A set of gene delivery vectors (lentiviral vectors, transposon-based delivery vectors) integrating the bacteriophytochrome associated diguanylate cyclase or the SEAP under the control of the $PIFN_{(ACD+)}$ were constructed (Table 1).

2.2. Engineering of NIR-dependent SEAP secreting cell line

To establish a cell line stably expressing the optogenetic pathway, the different vectors were integrated sequentially into the chromosome. First, a cell line expressing stably the photoactivable di-guanylate cyclase (DGC) was engineered by integrating the transposable gene cassette encoded on the pYH88 [11] (Fig. 2A). The gene delivery cassette encoding the photoactivable diguanylate cyclase BphS was integrated into hHMSC-TERT chromosome. The selected cell population was analyzed by transfecting the pSTING and pSO3 reporter and exposing the cells to 4 h NIR illumination (Fig. 1B). Furthermore, the polyclonal population expressing the optogenetic allele was sorted with fluorescence-associated cell sorting (FACS) using the mCherry fluorescent marker. The resulting clone library was propagated and screened by co-transfection with pSTING and the pSO3 SEAP reporter (Fig. 1B). The variability observed in the clone performance reflects the different transcriptional strength associated with the chromosomal integration loci. The best performing clone (clone 39) showing maximal NIR dependent SEAP secretion and low basal SEAP level in the dark was selected for further engineering. To characterize the NIR-photoactivable response, cells were illuminated with an increasing NIR-light regimen. The clone validation results show that the integration of the bacteriophytochrome tapping into the STING-TBK1-IRF3 axis was successful (Fig. 2B). In a second step, the polyclonal population expressing the photoactivatable diguanylate cyclase was transduced with lentiviral particles PSANTA encoding the SEAP reporter (LTR-$PIFN_{(ACD+)}$-SEAP-IRES-HO-1-P2A-SmurfP-LTR) (Table 1).

Table 1
Plasmid table.

Name	Description	Reference
pcDNA3.1 (+)	Constitutive PhCMV-driven mammalian expression vector (PhCMV-MCS-pA).	Invitrogen
pSEAP2-control	Constitutive mammalian SEAP expression vector (PSV40-SEAP-pA).	Clontech
pSTING	Constitutive mammalian STING expression vector (P_{hCMV}-STING-pA).	IMAGE: IRAVp968F0688D
pKZY121	Constitutive mammalian $DGCA_{CC3285}$ expression vector (P_{SV40}-$DGCA_{CC3285}$-pA).	[10]
PKZY113	Constitutive mammalian DGCL expression vector (P_{SV40}-DGCL-pA).	[10]
PSO3	$PIFN_{(ACD+)}$-driven SEAP expression vector ($PIFN_{(ACD+)}$-SEAP-pA). The IRF3 operator sites of $P_{IFN(AC+)}$ were space optimized.	[10]
PSO4	Constitutive mammalian DGCL expression vector (P_{hCMV}-DGCL-pA).	[10]
PSANTA	Lentiviral gene delivery vector encoding $PIFN_{(ACD+)}$-driven SEAP expression; (LTR-$PIFN_{(ACD+)}$-SEAP-IRES- HO-1-P2A-SmurfP-LTR).	This study
PFANTA	Lentiviral gene delivery vector encoding $P_{IFN(ACD+)}$.driven Human interferon-beta expression; (LTR-$PIFN_{(ACD+)}$.IFNβ- IRES-HO-1-P2A-SmurfP-LTR).	This study
PSBDGCL	Transposon gene delivery encoding EF1-A driven DGCL; (ITR; EF1a-DGCL-PA; RPBSA-BFP-ZEO-ITR)	This study
AAV1-IFN-ß	AAV1-IFN-ß	[49]
SBx100	Plasmid encoding the sleeping beauty transposase.	[50]
pCD/NL/BH*	HIV-1-derived GAG/Pol/TAT-encoding helper plasmid (P_{hCMV}-GAG-Pol-TAT-pA).	[51]
pLTR-G	Constitutive mammalian VSV-G expression vector (5'LTR-VSV-G-pA).	[52]
pYH88	Sleeping beauty Transposon vector encoding bacteriophytochrome BphS (ITR-PhCMV-BphS-P2A-YhjH-P2A-P65-VP64-NLS-BldD-P2A-mCherry-pA: PmPGK-PuroR-pA-ITR)	[11]

2.3. Characterization of the NIR-dependent SEAP secreting cell line

NIR-responsive sensitivity and performance of the resulting cell population integrating the bacteriophytochrome and the $PIFN_{(ACD+)}$ driven SEAP gene were determined for the isolated monoclonal population OGR3 clone 5, OGR3 Clone 7, OGR4 clone 39, OGR4 clone 2 (Fig. 2 **C)** and for the polyclonal population OGR3 (Fig. 2D, E). To confirm the non-toxic impact associated with constant NIR exposure, the viability of the engineered OGR3 cells was measured after 6 h NIR exposure; no adverse effects could be detected (supplementary Fig. 1). The stability of the expression was accessed by expanding the cell line over 15 passages (12 weeks) (supplementary Fig. 2). Despite some reduction in performance probably associated with the integration of the pCMV viral promoter (prone to epigenetic silencing) driving expression of the BPHS, the performance of the system remains efficient.

An experiment was designed to measure the transcriptional response of the OGR3 clone 5 upon NIR irradiation (Fig. 2F). RNA was extracted from the cells at different time points (0, 4, 16, 24, 48 h) after NIR induction of the system; key targets gene (SEAP, STING, TBK1, IRF3, IFN-ß, CXCL10, DGCL) expression was assayed by quantitative RT-QPCR (supplementary Fig. 3). SEAP mRNA rapid increase in transcription peaks at 4 h and is followed by the secretion of SEAP in the medium supernatant 16 h after the illumination (Fig. 2F). The expression level of the genes along the optogenetic pathway was analyzed. Parameters describing the synthetic optogenetic pathway activation were used to develop a simulation model of the recombinant SEAP expression. The model illustrates the dynamic of the NIR-controlled SEAP expression and secretion (Fig. 3). The observed dynamic suggests that an activation twice a week should be sufficient to maintain sustained secretion and diffusion the recombinant therapeutic protein over one week. After successful validation of the strategy to engineer hMSC-TERT OGR3 cells expressing the synthetic optogenetic network taping into the STING-TBK1-IRF3 axis to control SEAP secretion, a similar approach was applied to construct a recombinant IFN-β secreting cell; the Optoferon cell line.

2.4. The Optoferon cells engineering

To optimize the stability and reduce the basal activity of the NIR-photoactivable system, a DGCL allele that has reduced activity compared to the Bphs gene [29] was placed under the control of the Human EF1-alpha promoter in a transposable element gene cassette. Integration events were selected using the Zeocin resistant marker and positive clones sorted with the Blue Fluorescing Protein marker (BlueFP) using FACS. hMSC-TERT cells stably expressing the DGCL were further transduced with the lentiviral gene delivery vector pFANTA encoding the IFN-ß gene under the control of the $PIFN_{(ACD+)}$ promoter. The cell population performance was tested for NIR-dependent IFN-ß secretion **(**Fig. 4A**)** and expression stability **(**Fig. 4B**)**. The expression stability of the NIR synthetic pathway was confirmed by expanding testing the performance of the Optoferon cells over 12 passages (Fig. 4B). Proliferation and migration ability of the Optoferon cells were not affected by the engineering (supplementary Fig. 4).

2.5. Characterization of the Optoferon cell line

To monitor the impact of the activation of the synthetic optogenetic pathway controlling IFN-ß on other cytokines, the hMSC-TERT cells, the

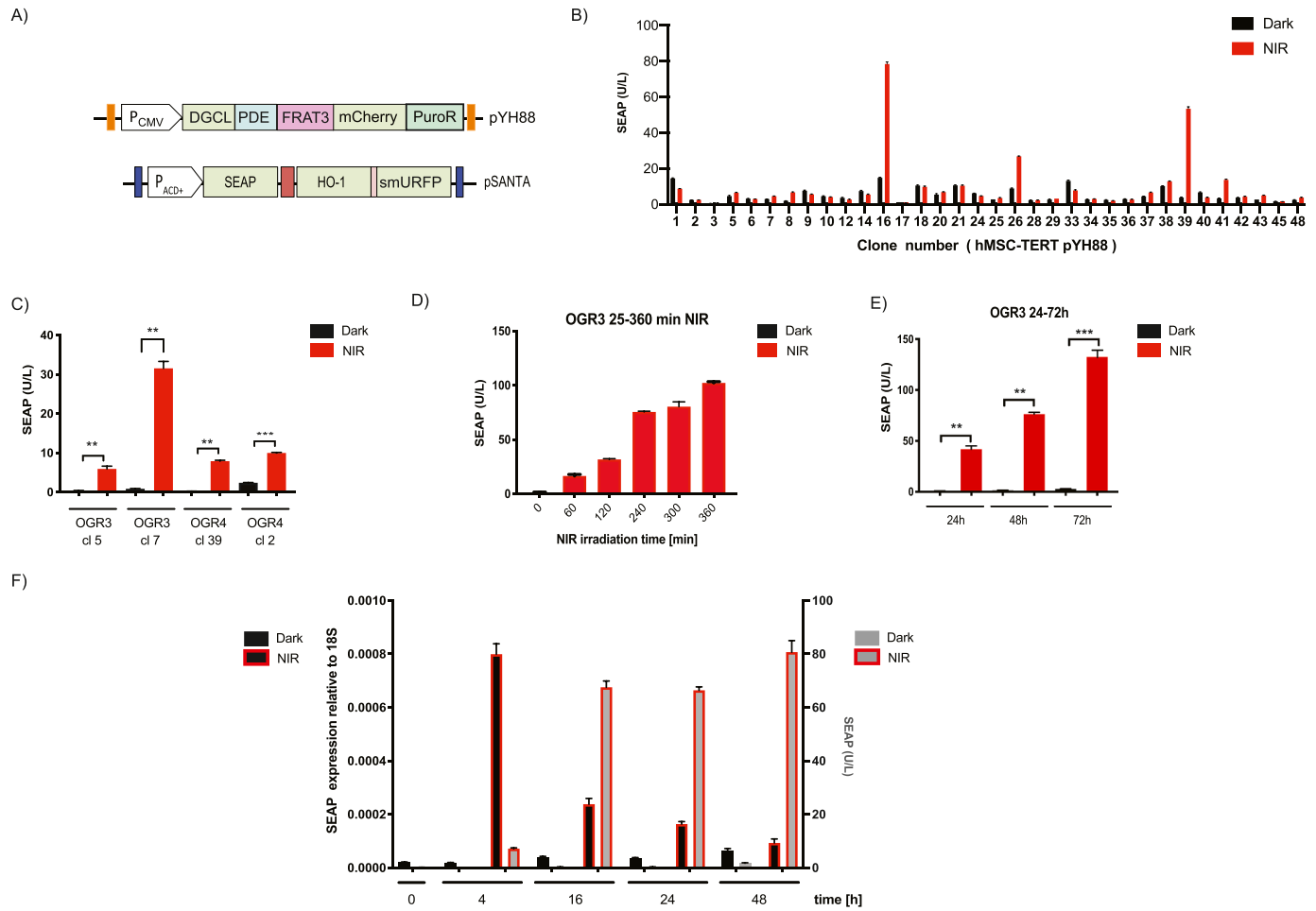

Fig. 2. (A) Schema of the genetic constructions encoding the optogenetic pathway. (B) Clone profiling, DGCL integrated hMSC-TERT clonal population transfected with pSO3 (PIFN$_{(ACD+)}$-SEAP-pA) reporter. Cells were exposed to 4 h NIR, and SEAP (U/L) scored in the medium supernatant 48 h after. The clone 39 and clone 16 show the best performance. (C) PYH88/ pSANTA integrated in clone 39 in the presence and absence of 4 h NIR light; SEAP (U/L) is scored 48 h after in the medium. (D) OGR3-Clone 7 NIR Dependent SEAP expression, cells are exposed to an increasing light regimen, secreted SEAP (U/L) is scored 48 h after. (E) OGR3-clone 7 SEAP secretion in presence and absence of 4 h NIR light, medium supernatant collected at 24 h, 48 h, and 72 h, and scored for SEAP (U/L) activity. (**F**) ORG3-Clone 7 SEAP mRNA profiling with relative gene expression relative to 18S ribosomal RNA gene and scoring of secreted SEAP (U/L) in the medium supernatant. An experiment performed in dark or with 4 h NIR exposure. Samples were taken at 0, 4, 16, 24, 48 h. SEAP RNA relative to 18S black left axis in black shaded column (Dark), black column red shaded thick line (NIR 4 h), SEAP activity right axis in (U/L); grey column (Dark), grey shaded column thick red line (4 h NIR). (For interpretation of the references to colour in this figure legend, the reader is referred to the web version of this article.)

DGCL expressing cells, and the Optoferon cell line, were profiled for the secretion of inflammatory cytokines in the presence and absence of NIR-light stimulus. Secreted Interferon beta is only detected with the cell line integrating the IFN-beta transgene (**Fig. 4C**). The Optoferon cells secretes secrete low level IFN-beta in the dark (< 50 pg /mL) and above 1000 pg/mL interferon after induction. Detection of secreted IL-8 in the parental hMSC-TERT cell line is independent of the integration of the optogenetic pathway. In contrast the cytokine profile of the Optoferon cells observed upon NIR activation reflects the cyclic di-nucleotide (CDN) mediated activation of the STING-TBK1-IRF3 axis (Fig. 4C, D) [30]. Upon 4 h NIR Illumination of the Optoferon cells, we observe the induction of the cytokine RANTES (Regulated on Activation, Normal T-Cell Expressed and Secreted) and IP10 (CXCL10). It was previously reported that RANTES is induced by cytosolic CDN [30]. Thus, RANTES secretion is only detected when the cell line integrating the photoactivable diguanylate cyclase DGCL is exposed to NIR light [30]. CXCL10 a marker of IFN-beta efficacy [31,32] is only detected in the cell line integrating the human IFN-β gene under the control of the pIFN$_{(ACD+)}$ promoter resulting from downstream IFN signaling. In contrast to RANTES, CXCL10 secretion can also be detected in the dark, this suggest that the low basal secretion (in the dark) of the recombinant interferon beta triggers some IFN-beta dependent pathway.

RNA extracted in different conditions, in presence or in absence of 4 h NIR-induction (0, 2 h, 2 h15, 2 h30, 4 h, 4 h15, 4 h40 min) of the Optoferon cells line were profiled using the new generation sequencing (NGS) method. While a slight increase of IFN-β after 2 h30 NIR induction, a considerable increase was noticed after 4 h NIR exposure. The comparison between the transcriptomics of the hMSC-TERT non-engineered cells and the Optoferon cells in the dark condition show that despite a basal increase in the interferon-β mRNA, the transcriptional activity of the interferon regulatory factors (IRF 1–8) was not affected. No significant transcriptomics changes were observed when the hMSC-TERT cells were exposed to 4 h NIR light (Fig. 5) confirming the innocuity associated with low power NIR light.

In contrast, the comparison between the Optoferon cells transcriptomics of 4 h NIR exposure to the dark control show the most significant changes. Type-I interferon beta, 2–5 Oligoadenylate synthase like protein (OASL), histone cluster protein [33], Interferon-inducible T-cell alpha chemoattractant CXCL11; RANTES (CCL5); Interferon Induced protein with Tetratricopeptide repeats IFIT1, IFIT2, IFIT3 are among the most upregulated genes (Fig. 5A, B). In contrast, CXCL8 and a set of non-coding long RNA transcripts are downregulated upon NIR

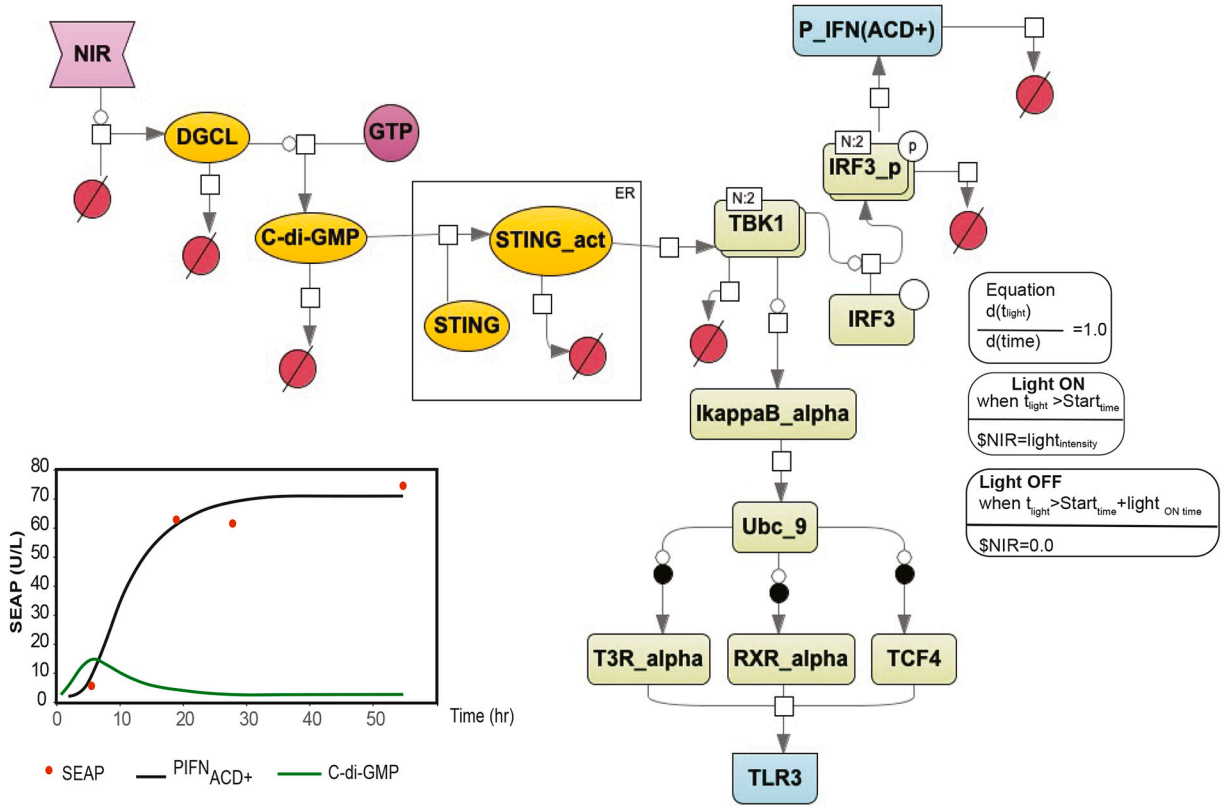

Fig. 3. Synthetic optogenetic pathway model; this representation is given in accordance with commonly accepted SBML (Systems Biology Markup Language) and SBGN (Systems Biology Graphic Notation) standards. Nir light (NIR) activates the diguanylate cyclase (DGCL) that generates *C*-di-GMP and activates STING. STING mediates the TBK1-IRF3 axis activation and triggers recombinant interferon promoter ($PIFN_{ACD+}$) expression. The small ubiquitin-like modifier (SUMO) E2 enzyme UBC9 specifies the Thyroid receptor 3 alpha (T3R_Alpha), the retinoic acid receptor alpha (RXR-Alpha), and subsequently the Toll-like receptor 3 (TLR3) pathway. Simulation model of NIR induced SEAP expression, integrating cyclic-di-GMP and $PIFN_{ACD+}$ expression; SEAP (U/L) experimental values as a red dot. (For interpretation of the references to colour in this figure legend, the reader is referred to the web version of this article.)

illumination and subsequent interferon-beta secretion.

The expression data were further processed using an upstream analysis [32] to identify the master regulators potentially coordinating the NIR response. This approach comprises two major steps: (i) integrating the signaling promoters and enhancers of differentially expressed genes for the transcription factors (TFs) involved in their regulation and, thus, important for the NIR activation process; (ii) reconstructing the signaling pathways that activate these TFs and identifying master regulators. For the first step, the database TRANSFAC [34] is employed together with the TF binding site identification algorithms Match and CMA [35] and genome enhancer software (https//genexplain.com/genome-enhancer) [36].

Comparing the results for samples of light-induced engineered cells, it was concluded that while the effect of induction is noticeable at 2 h, the complete activation of the pathway seems to be achieved only at 4 h. This is consistent with model simulation results, which predicted some delay before the complete activation of the pathway. On the other hand, at 4 h the genome enhancer analysis explicitly detected interferon signaling pathways from interferon induced IFIT1, IFIT2 (Fig. 5A, B). Furthermore, the mapping of the differentially expressed gene to the TRANSPATH gene ontology suggests that the system was also activating through IκBα the TLR 3 pathway (Fig. 5, C).

2.6. Cell-scaffold for supporting growth in the cell chamber

Experiments to validate the transfer feasibility of the optogenetic programmed cells from in-vitro culture conditions as a cell monolayer to the tissue-like growth conditions on cell scaffolding material using the Optoferon cells (hMSC-TERT-DGCL-pFANTA) were established. The microscopic observation confirmed that a 3D growth like structure was observed when the concentration of the cell scaffold was above 50%. 50% scaffold concentration was selected for the implantation protocol. NIR illumination and medium changes were also evaluated for their ability to support 3D growth conditions (supplementary Fig. 4).

2.7. Wireless powered implant system requirements

Validation of the NIR-LED light source component to be integrated into the optoelectronic interface was performed using different 700 nm LED packages, from high power-LED source to lower power surface-mount technology (SMT) components (Fig. 6A, B, C). HEK293-T cell line transfected with the system components (DGCL, STING, SEAP reporter) were exposed to 3 h illumination. The packaging of the LED components and the position of the LED did not affect the system performances (Fig. 6B). A small surface mount devices (SMD) package was selected for further evaluation. Different currents were tested to evaluate the minimal power needed to activate the optogenetic system (Fig. 6C). The experiment shows that a minimum of 10 mA power (1 mw/cm^2) is required to activate the system, furthermore that an induction time of 16 h was equivalent to 3 h at 60 mA powering. The illumination condition is not comparable to therapeutic usage of class IV light therapy NIR laser (>500 mW/cm^2).

To validate the implant optoelectronic interface requirements, 3D printed technology was used to generate the casing integrating the optoelectronic. The device architecture was defined with a cell chamber having dimensions 15*20*0.6 mm (W*L*H) surrounded by an energy-harvesting antenna powering the optoelectronic rectifying circuit. The cell chamber confinement barrier is composed of a hydrophilic

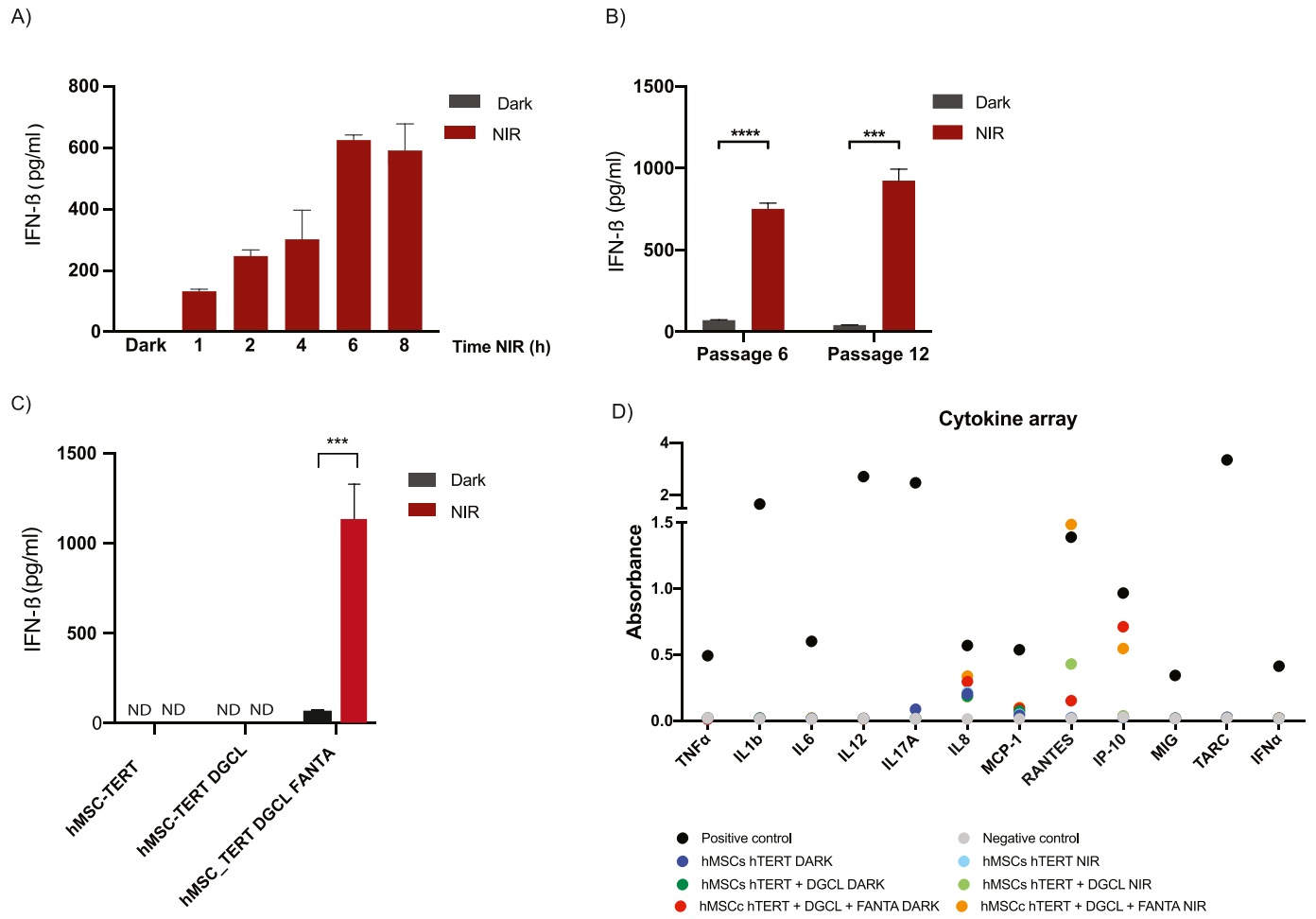

Fig. 4. (A) Optoferon cell line, NIR dependent secretion of INF-ß, cells were exposed to 1, 2, 4, 6 and 8 h of NIR light or kept in dark. Interferon-beta is scored in the medium by enzyme-linked immunosorbent assay 40 h after illumination. (B) Stability of NIR-dependent IFN-ß secretion over 6 and 12 passages of the Optoferon cell line. Cells were exposed to 4 h NIR and SEAP was measured in the medium supernatant after 48 h. (C) Detection of NIR-dependent secretion of interferon in the parental cells hMSC-TERT, the hMSC-TERT-DGCL, and the recombinant IFN producing cells hMSC-TERT DGL FANTA. Cells were exposed to 4 h NIR light and IFN-ß scored in the medium supernatant and after 48 h. (D) Cytokine array performed on the parental cells hMSC-TERT, the hMSC-TERT DGCL, and the recombinant IFN producing Optoferon cells (hMSC-TERT DGCL FANTA) exposed to NIR light for 4 h. Absorbance indicates the level of detection of control. Elisa plate provided coated with specific cytokine capture antibodies are used for the assay. The positive controls are made by loading the standard antigen mix provided by the assay manufacturer, and negative control is made by adding the control medium supernatant.

polypropylene 0.45 μm membrane and rigidifying 100 μm polypropylene mesh glued on cell chamber frame (600 μm) (Fig. 6D).

2.8. Biocompatibility and surgical implantation

A series of prototypes cell chamber compartments were 3D printed for estimating the biocompatibility, the optimal growth conditions inside the cell chamber. A cultivation cell chamber was designed with one semi-porous hydrophilic membrane side, and with an opposite side assembled using an optically transparent material (Veroclear, PolyJet photopolymer). The optical window of the cell chamber enables the in vivo visualization of the cells growing in the device [37]. The ergonomics of the casing was refined to limit sharp edges.

The cell chamber components were assembled by gluing the laser-cut membranes to either an injected polypropylene or a photopolymerized casing. The gluing assembly process offers more reliability in the assembly rather than direct over-molding the membrane on the frame as it preserves the membrane integrity. To confirm surgical procedure and biocompatibility of the materials implants were placed subcutaneously in mice for pilot experiments.

The surgical implantation approach was validated with implants (without cells) placed subcutaneously on the lower back of mice for two weeks implantation [37]. Mouse tissue at the implantation site was analyzed by microscopic analysis of stained tissue (histology**).** An objective analysis followed by hematoxylin and eosin staining has been performed to assess the mouse tissue at the implantation site [37]. The analysis confirmed that no acute inflammatory response was detected and that after two weeks of implantation, a neovascularization was observed in the tissue engraftment site (Fig. 6E, F).

The cell chambers were assembled, sterilized and loaded with cell lines expressing NIR-fluorescing protein. Prior ex-plantation, mice having subcutaneous implant cell chamber containing NIRFP expressing cells were imaged in-vivo. The analysis shows that cells expressing a NIR-fluorescent reporter in the implant confinement cell chamber were viable. Neovascularization was observed in the tissue engraftment site ten days after the implantation (Fig. 6E, F). The experiments confirm that the cell loading process in the implant cell chamber did not affect the cell viability in vivo. Detailed report of the biocompatibility study was reported elsewhere [37].

Examination of the implantation site revealed the presence of some fibrotic tissues after two weeks. The immune-mediated foreign body response may impair the survival of certain grafted cell lines [38]. To integrate into the implantable device design, an option to prevent the formation of fibrotic capsule formation a proven antifibrotic strategy

A)

ID	Gene symbol	Gene description	logFC	logCPM	P-alue
ENSG00000171855	IFNB1	interferon beta 1	1.84	5.51	9.75E-93
ENSG00000277224	HIST1H2BF	histone cluster 1 H2B family member f	1.69	1.22E-2	6.14E-3
ENSG00000203814	HIST2H2BF	histone cluster 2 H2B family member f	1.42	1.58	3.25E-3
ENSG00000235064	SLC25A5P2	solute carrier family 25 member 5 pseudogene 2	1.3	0.66	3.62E-5
ENSG00000119922	IFIT2	interferon induced protein with tetratricopeptide repeats 2	1.23	8.62	2.41E-80
ENSG00000273802	HIST1H2BG	histone cluster 1 H2B family member g	1.21	1.66	3.04E-3
ENSG00000184678	HIST2H2BE	histone cluster 2 H2B family member e	1.2	5.12	1.22E-3
ENSG00000135114	OASL	2'-5'-oligoadenylate synthetase like	1.11	5.35	2.45E-43

B)

ID	Title	Number of hits	group size	Expected hits	P-value	Adjusted P-value	Hit name
918299	R-HSA-909733: Interferon alpha/ beta signaling	2	26	0.03238	3.34E-04	0.00134	IFIT1, IFIT2
921151	R-HSA-915331: Interferon signaling	2	43	0.05355	9.23E+00	0.00185	IFIT1, IFIT2
1280225	R-HSA-1280215: Cytokine signaling in immune system	2	226	0.28144	0.02467	0.03289	IFIT1, IFIT2

C)

ID	Title	Number of Hits	Group Size	Expected hits	P-Value	Adjusted P-value	Hit Name
CH000000278	CH000000278	1	2	0.00781	0.0078	0.07782	MITF
CH000000775	RANKL ---> MITF	1	10	0.03905	0.03844	0.10251	MITF
CH000000777	poly(I:C) ---> IRF-3	1	3	0.01171	0.01167	0.07782	TLR3
CH000000819	dsRNA ---> IRF-7:IRF-3:CBP:p300	1	8	0.03124	0.03086	0.10251	TLR3
CH000000859	p38alpha ---> MITF	1	3	0.01171	0.01167	0.07782	MITF
CH000003741	cholesterol ---> chelate	1	8	0.03124	0.03086	0.10251	HSD3B7
CH000003747	classic or neutral bile acid metabolism	1	9	0.03514	0.03466	0.10251	HSD3B
CH000003891	RANKL ---> CATH-K	1	10	0.03905	0.03844	0.10251	MITF
CH000004453	MITF ---> TPH1	1	6	0.02343	0.02322	0.10251	MITF
CH000004469	IL-3 ---> STATS	1	7	0.02733	0.02705	0.10251	IL3RA
CH000004614	Tie2 dephosphorylation	1	3	0.01171	0.01167	0.07782	PTPRB
CH000004623	MIC2-isoform2 ---FosB---> MMP9	1	9	0.03514	0.03466	0.10251	FOSB
CH000004624	MMP9	1	7	0.02733	0.02705	0.10251	FOSB
CH000004665	FN1	1	3	0.01171	0.01167	0.07782	ETS1
CH000004671	HIF2	1	3	0.01171	0.01167	0.07782	ETS1

Fig. 5. (A) Top induced gene upon 4 h NIR induction of the Optoferon cell line. (B) Pathway analysis results Interferon pathway after 4 h NIR. (C) Mapping to Reactome pathway database/TRANSPATH Ontologies of differentially expressed gene after 4 h NIR.

was tested [38]. GW2580 a colony-stimulating factor 1 receptor (CSF1R) inhibitor acting as an antifibrotic compound was selected to be slow-released from the silicon layer used to manufacture the device. Crystallized drug formulation of GW2580 was integrated into a silicon layer of the device. Mice were implanted with GW2580 releasing devices for four months, a histologic examination performed after explantation confirmed that in such conditions no fibrotic capsule was present in the implantation site (Fig. 6G-J). These results confirm the possibility to integrate into the implant an antifibrotic strategy compatible with the device manufacturing process.

2.9. Device performance in vivo

Cell-based devices integrating the wireless powered optoelectronic circuit were validated in-vitro. It was observed that the interferon secretion performance of the activated devices was increasing over time, as Optoferon cells proliferate into the implant cell chamber (Fig. 7D, E, F). The devices were fully responsive after a week. Repeated induction of a device could be monitored with up to five iterations of the induction in a month (supplementary Fig. 5).

To validate the Optogenerapy device requirements in vivo for light-controlled cytokine delivery, the EAE mice a well-known model of multiple sclerosis was selected [25]. Photopolymerized implant casing integrating PCB optoelectronic and cell chamber loaded with Optoferon cells were implanted in female mice before induction of the disease model. Female cohorts are preferred because EAE male mice do not develop neuropathic pain-like behaviors associate with EAE pathology. It was established that the surgical implantation procedure of the device in EAE mice pre-implanted animal model of multiple sclerosis did not alter the observation of the EAE clinical score [37]. To facilitate the validation of the Optoferon cells loaded device with the EAE mice model, it was decided not to include GW2580 during manufacturing in the silicon of the device, as antifibrotic compound has demonstrated effect on microglia [39] and thus could influence the validation of the therapeutic efficacy of the Optoferon cells in the EAE mice model.

Two weeks after implantation of the device, EAE induction was performed in all mice. To monitor the evolution of the disease progression, a daily evaluation of the EAE neurological score was performed. At the onset of the first symptoms (i.e., 6 days after immunization), the device of the IFN treatment group (EAE + Implant ON) mice was wirelessly activated with a regimen of 6 h twice per week. To evaluate the efficacy of the Optogenerapy strategy a control group was done with a gene therapy approach based on adeno-associated viruses expressing the human interferon beta was selected [49]. The gene therapy approach was preferred as comparator over repeated intravenous injection as it relies on in-situ expressed interferon and for ethical reasons to avoid daily administration in mice already affected. The AAV1-IFN-β positive control treatment EAE mice group (EAE + AAV1-IFN-β) was retro-orbitally injected with an adeno associated virus expressing the human interferon-beta AAV1-IFN-β (1.6 10e11 total vg) (Fig. 8A).

Detection of the peak of EAE symptoms occurred at 9–11 days for the EAE group with a mean maximum severity score of 2–2.5. The first peak was followed by a recovery after 2–3 days. A second increase of the paralytic score was observed at around 15–17 days; a 1.5 severity score was observed until the sacrifice of the animals. For the AAV-treated control group (EAE + AAV1-IFN-β group), a similar manifestation of the EAE was observed but the severity of the second paralytic score was weaker. Due to the time window to allow an effective expression of AAV transgene expression of about 2 weeks, the beneficial effect of the IFN delivery control could be observed only at the time of the second paralytic score. For the control group of non-activated implanted

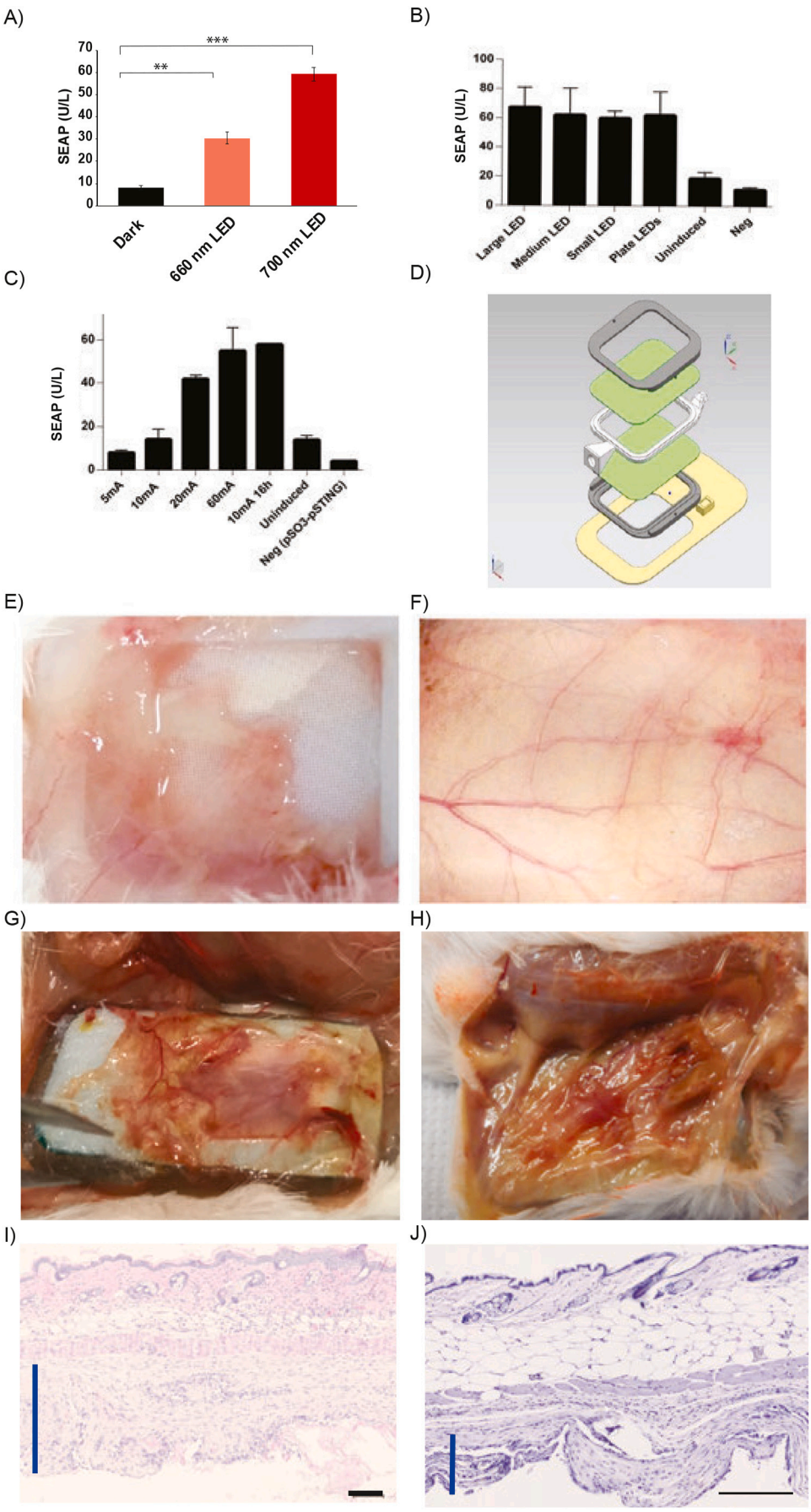

Fig. 6. (A) Comparison of LED wavelength 660 nm and 700 nm for NIR-dependent SEAP production. HEK293T cells transfected with DGCL expression plasmid PKZY113 (P_{SV40}-DGCL-pA) and the PSO3 SEAP reporter plasmid ($PIFN_{(ACD+)}$-SEAP-pA) were exposed to 90 min NIR light. The SEAP was scored 48 h after in the medium supernatant. (B) HEK293T cells transfected by PKZY113 (P_{SV40}-DGCL-pA) and the SEAP reporter PSO3 ($PIFN_{(ACD+)}$-SEAP-pA) plasmid were exposed to different 690 nm LED packages for 90 min. The SEAP was scored 48 h after in the medium supernatant. (C) HEK293T cells transfected with PKZY113 and PSO3 SEAP reporter plasmid were exposed 90 min (otherwise mentioned) to different NIR powering intensity. The SEAP scores 48 h after in the medium supernatant. (D) Exploded 3D sketch view of the Optogenerapy device. The over moulded implant architecture is composed of (from top to bottom): upper cell chamber casing; membranes 100 μm polypropylene mesh above the cell chamber semi-porous membrane; 600 μm thick spacer light guide; lower cell chamber casing; flexible optoelectronic circuit and energy harvesting antenna. (*E*-F) Implant explanted after 2 weeks, neovascularization of the cell chamber. (G-H) Explantation of implants after 4 months; (G) implant uncoated or (H) coated with antifibrotic compound GW2580. (I-J) Hematoxylin-eosin of skin section in implanted mice; (I) without antifibrotic coating, (J) with antifibrotic coating, scale bar represents 200 μm.

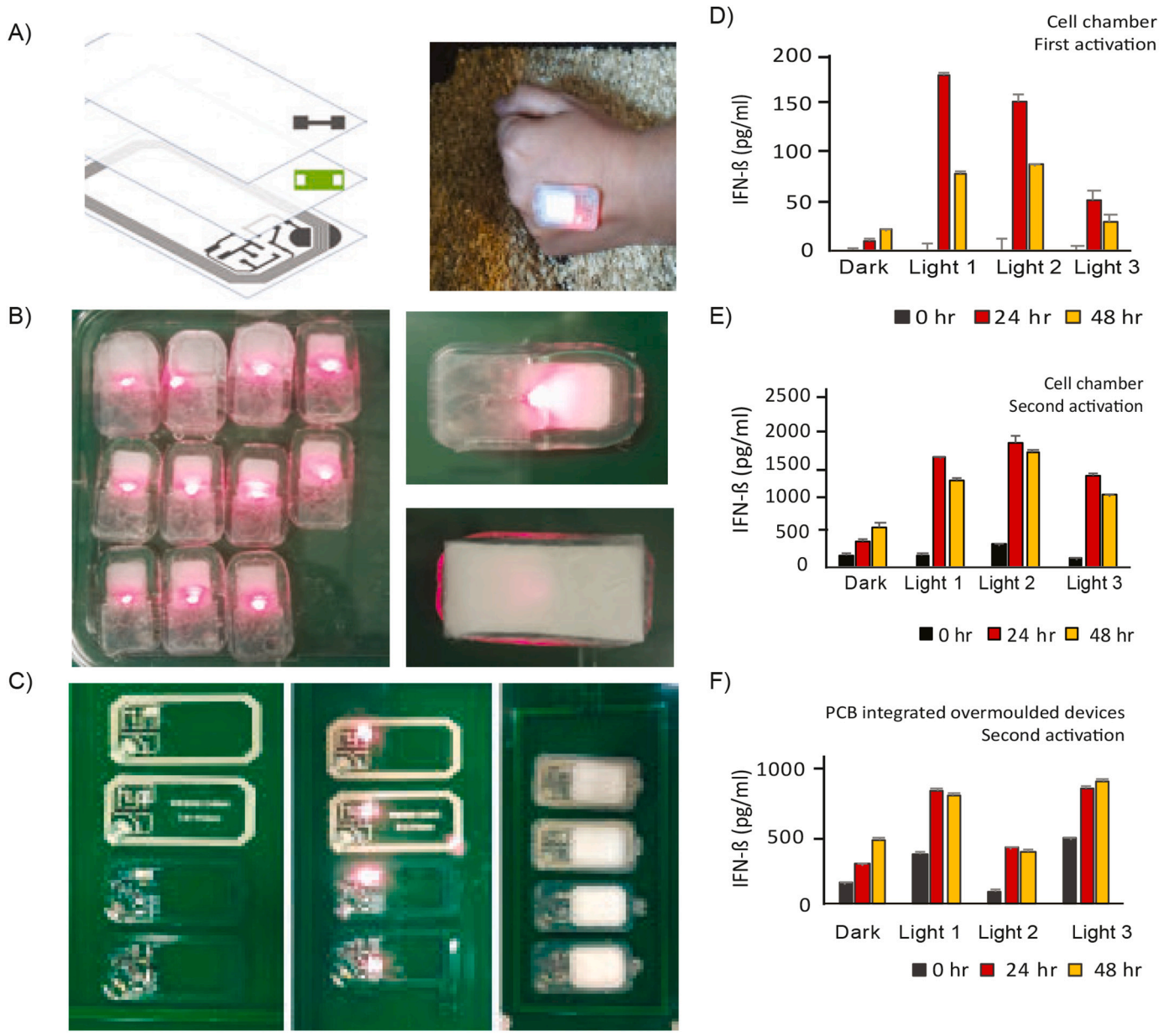

Fig. 7. (A) Flexible optoelectronic circuit integrating an energy harvesting antenna; top layer connection between antenna poles and optoelectronic, middle layer insulating layer, bottom layer optoelectronic circuit. (B) Batch production of PCB integrating device, top view of the optical window, bottom view membrane. (C) Industrial manufacturing integration of PCB and flexible inject printed optoelectronic circuit with LED in different orientations. Integration of the cell chamber by silicone molding. (D) Batch testing of cell chamber module after one week incubation; (E) after two weeks incubation. (F) Batch testing of silicon over moulded devices integrating flexible screen-printed optoelectronic circuit after two weeks incubations. Devices loaded with the Optoferon cells are activated with wireless power for 6 h and the IFN-ß is scored in the medium supernatant at induction time 0 h, 24 h with medium exchange, 48 h with medium exchange.

animals (EAE + Implant OFF), the first peak of EAE symptoms was observed at 10–12 days with a mean maximum score of 1.5–2. The second paralytic score was observed at the sacrifice of the animals. In comparison to the non-treated group (EAE), a delay in the paralytic score peak was observed most probably resulting from the low basal secretion of interferon-beta from non-activated devices. For the treatment group (EAE + implant ON) the EAE score peaks at 10–12 days with a mean maximum score of 1.5. In contrast to the EAE control group, no occurrence of a second peak could be observed. The severity score remained between 0.5 and 1.5 until the sacrifice of animals. This score was significantly decreased between 19 days and 22 days for the different groups of mice (EAE implant ON vs EAE). These observations confirmed that despite some basal IFN secretion, the activation of cells residing in the devices before the appearance of the second peak of the disease further improves the neurological score (Fig. 8A).

During the manifestation of the EAE, mice CNS undergo a characteristic myelin degeneration. To evaluate the efficacy of the bioelectronic device activation on the prevention of spinal cord injury, post sacrifice histologic analysis of the myelin section was performed (Fig. 8D,C). Spinal cord myelin sections were stained with Luxol (Fig. 8B). A significant demyelination was observed in the EAE control group in comparison to WT mice, indicating the characteristic onset of the EAE disease. Similarly, demyelination was observed in the non-activated EAE + implant OFF group. Importantly, myelin level monitored in the treatment group (EAE + Implant ON) mice was like the one detected in the WT mice group and similar to the AAV control group expressing recombinant interferon, confirming the protective effect of in-situ delivered interferon beta. The results indicates that

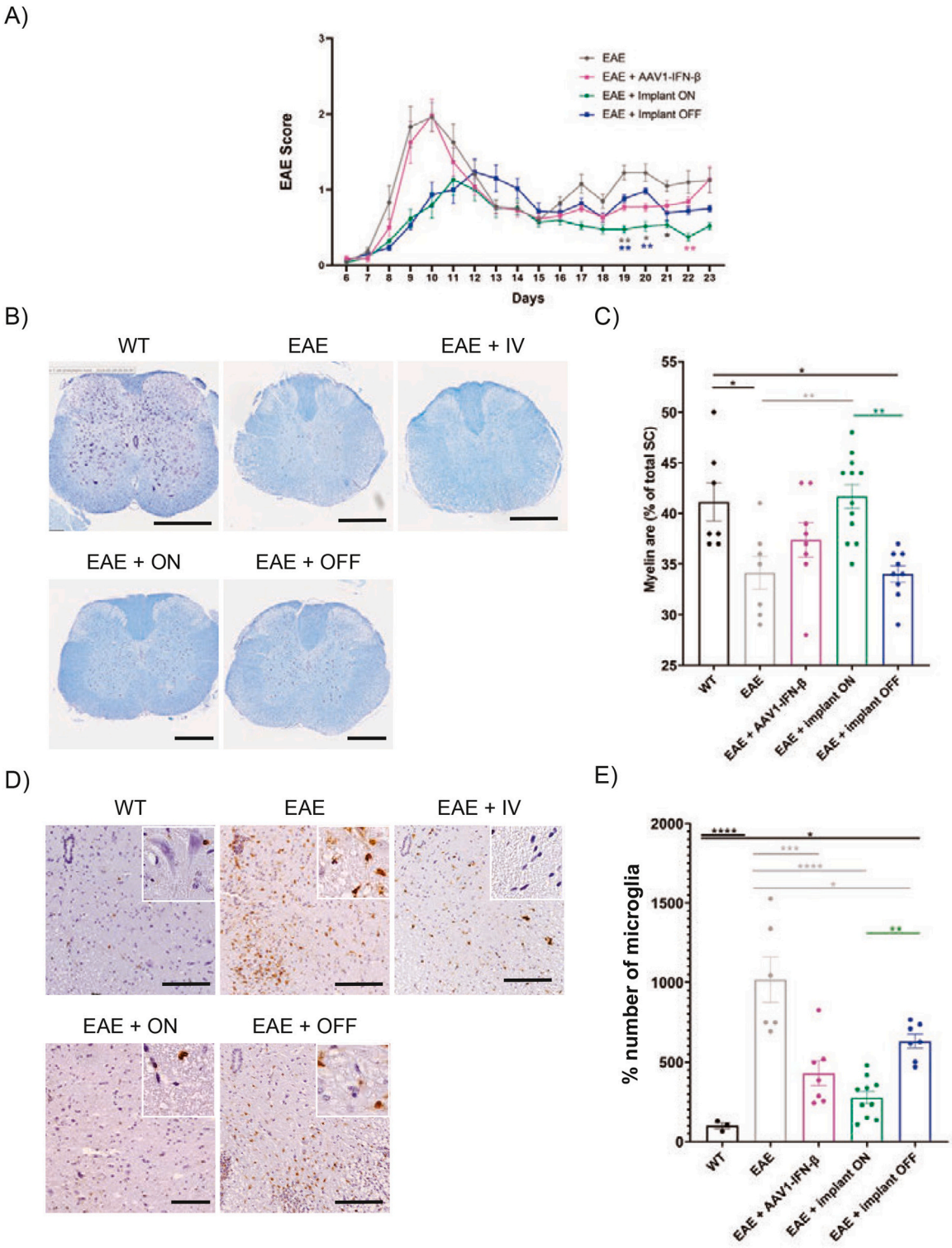

Fig. 8. (A) EAE mice implanted with Optogenerapy device programmed with optoferon cells over 26 days. Comparison of EAE mice scoring with no device (EAE, $n = 12$), mice transduced with an AAV1 expressing IFN-ß ($n = 14$), EAE mice implanted with the device not activated EAE implant OFF ($n = 20$) and EAE implant ON ($n = 22$) (6 days after immunization), device of the treatment group (EAE + Implant ON) with a regimen of 6 h twice per week. (B) Representative image of post sacrifice histologic analysis of the myelin section; (WT) control mice; (EAE), EAE control mice; (EAE + IV), EAE mice group injected with AAV1-IFN-ß; (EAE + implant ON), mice group implanted with the bioelectronic device loaded with Optoferon cells and device activated; (EAE + implant OFF), mice group implanted with the biolectronic device loaded with Optoferon cells, device not activated. (C) Myelin level, lumbar spinal cord myelin area integrated in percentage compared to the WT myelin level. (D) Representative image of post-sacrifice histologic analysis of the neuroinflammation scoring the microglia specific marker Iba-1 (IBA-1 antibody); (WT), control group WT mice; (EAE), control group EAE mice; (EAE + IV), EAE mice group treated with AAV1-IFN-ß; (EAE + ON), mice implanted with the biolectronic device loaded with Optoferon cells device activated; (EAE + OFF), mice implanted with the Optogenerapy device loaded with Optoferon cells device not activated. (E) Percentage of microglial cells, number of Iba-1 positive cells on area integrated on the lumber spinal cord in percentage compared to the WT.

Optogenerapy treatment significantly prevent acute demyelination and is as efficient as control treatment with in situ expression.

Moreover, spinal cord sections were stained with the ionized calcium binding adaptor molecule 1 (Iba1), a microglia specific marker to evaluate the efficacy of cell-based bioelectronic devices on the prevention of neuroinflammation (Fig. 8D,E). As expected, significant neuroinflammation was observed in the EAE control group in comparison to WT mice, characteristic of the EAE disease as well as in the non-activated EAE + implant OFF group. In contrast, EAE + implant ON shows similar inflammation level as the control WT group like the EAE + AAV1-IFN-ß group thus demonstrating the clear benefit of the treatment on neuroinflammation.

2.10. The device biocompatibility in implanted EAE mice

As observed with NiRFP expressing cells loaded device, no signs of severe inflammation, nor muscular degeneration or dilation of adipose tissue were observed on the tissue at the implantation site of the EAE mice (supplementary Fig. 5). As reported for macro encapsulation devices having similar flat-sheet cell chamber architecture [12,13] neovascularization was observed at the cell chamber location (supplementary Fig. 5F). Moreover, to assess the cell viability in the device, cells contained in the explanted device were recovered. The Optoferon cells from the explanted devices (supplementary Fig. 6) show cell viability superior to 50% estimated by trypan blue [37]. In the animals that were subjected to AVV1-HumIFNβ injection, the liver was analyzed. Hematoxylin-eosin staining on the liver section did not reveal toxicity (supplementary Fig. 5G). Also as previously reported, all EAE mice show significant splenomegaly due to the immunization [40]. Hematoxylin-eosin staining on the spleen section shows a massive lymphocyte infiltration in different groups (supplementary Fig. 5G).

2.11. Industrial manufacturing of bioelectronic cell-based devices

After the Optogenerapy device requirements were validated for the controlled delivery of IFN-β in the multiple sclerosis EAE animal model. The cell chamber materials and components complying with implantable medical device guidelines (USPVI grade) were integrated into the manufacturing process. Having established a successful 3D manufacturing strategy, an approach integrating the PCB optoelectronic board, with the cell chamber into a silicon over-molding process was established. It allows the integration of the device components with USPVI grade over-molding silicone with a liquid silicon rubber (LSR) injection molding machine in a cleanroom. Two manufacturing routes were explored; the first one integrates a PCB circuit supporting the electronic into the device (Fig. 7B,C), the second capitalizes on a flexible screen-printed optoelectronic circuit [18,41] (Fig. 7C). The strategy of the flexible device is based on a flexible energy harvesting antenna connected to the optoelectronic rectifying circuit (Fig. 7.A). The utilization of a sandwich-insulated and conductive ink-printed flexible layer enables the antenna powering circuit to operate (Fig. 7A) at 10 cm through the skin. The assembled device is over-moulded with silicon.

A second strategy capitalizes on integrating the optoelectronic on a PCB in a 3D-printed casing. The cell chamber is semi-transparent and allows direct visualization of the cells (Fig. 7.B).

The devices were manufactured, and their performances validated with the Optoferon cells (Fig. 7D, E, F). Envisioning a step forward beyond the conventional PCB manufacturing path in personalized medicine, a 2D flexible, soft, and wearable electronic circuit was prepared. The assembly of the flexible optoelectronic circuit uses a combination of screen-printing technology with surface mount devices (resistors, capacitor, diodes, and LED) using pick-and-place technology, to operate as transcutaneous wireless power transmission [41] (Fig. 7A) with the goal of obtaining a thinner, seamless, lightweight and conformable implantable device. Screen printing of silver nanoparticle conductive inks was chosen as the most suitable technique for the inductive link circuit. Using this technology, the process temperatures for circuit fabrication are below 120 degrees Celsius, allowing the use of polymers as substrates such as polycarbonate (PC) or polyethylene terephthalate (PET), among others, when compared to glass-reinforced epoxy laminate material (FR4). This advantage also increases the material compatibility to injection molding materials, either silicones or thermoplastics. Importantly, the use of low temperature silver nanoparticle inks and adhesives in printing and pick-and-place technologies supports high-throughput and low process variation with equipment's already utilized in conventional circuitry manufacturing, and capacity to print high resolution thick conductive tracks (15 μm) required for printed antennas.

The manufactured implant batch functionality is validated by controlling LED performance and loading Optoferon cells and the basement membrane matrix scaffolding material in the sterilized manufactured device. Devices immersed in growth medium are wirelessly activated once a week. The IFN-β scoring is performed in the implant surrounding milieu (Fig. 7F, supplementary Fig. 7). The results confirm that the established device manufacturing paths can support further dissemination of the Optogenerapy technology preclinical development and its translation to the clinic.

3. Discussion

Cell-based drug delivery device technology is moving to the clinics [5,42]. The technology offers an alternative advanced therapeutic strategy to treat macular degeneration [43], diabetes [44,45] but also can act as anti-cancer vaccines [46]. Implantable cell-therapy devices are composed of a cell chamber integrating a semi-porous membrane to provide an interface between the therapeutic cells and the implantation site. Progress made in synthetic biology using optogenetic tools supports the genetic programming of light-controlled therapeutic cell lines [8,10,29]. The integration of a synthetic NIR-optogenetic pathway (Fig. 1A) in immortalized human Mesenchymal stem cells hMSC-TERT [47] offers combined advantages to rely on a validated therapeutic cell-line and a robust NIR-actuated gene network. In contrast to other encapsulated therapeutic cell lines, the NIR-interface programmed cells offer a unique electronic control over the secretion of the therapeutic protein. An inherent challenge in the dissemination of an advanced bioelectronic device is the integration of intricate requirements combining the genetic programming of the therapeutic cells with the complex medical electronic manufacturing [18,41]. Our work set the bases for the industrial manufacturing of wireless-powered implantable cell-based medical devices integrating state-of-the-art manufacturing technics (ie; SLT photopolymerization, injection molding, and flexible electronics) [18] (Fig. 6-7). The validation of the manufacturing steps supports the translation of the bioelectronic cell therapy vehicle strategy to deliver IFN-β in the animal model of multiple sclerosis (Fig. 8). Furthermore, the modular technology integrating photoactivable secretory pathways with optoelectronics qualifies the bioelectronic hardware as an open platform to develop other therapeutic protein delivery applications.

As validation of the genetic engineering strategy, in-depth characterization of the Optoferon therapeutic cell line was performed by global transcriptional analysis and cytokine profiling. The analysis shows how the integrated photoactivable di-nucleotide synthase tap-in the native interferon signaling pathway where STING integrates the surge of cyclic di-nucleotide (*C*-di-GMP) to activate IRF3/TBK1 dependent type-I interferon pathway (Figs. 3,5). NGS performed on the NIR activated Optoferon cell lines recapitulates the STING dependent transcriptional activation of the IFN-β pathway and as a large amount of interferon is produced, illustrates the activation of IFN-β dependent system (Fig. 3) [48]. While induction of STING-dependent cytokine is observed in the medium, except RANTES; no other NIR-dependent cytokine is detected. Also, we noticed that integrating the bacteriophytochrome lead to noticeable increase in the $PIFN_{(ACD+)}$ driven expression. As previously

observed for the HEK293 cell lineage, the activation of the interferon pathway does not result in the measurable secretion of native interferon while increased induction of its mRNA is noticeable by NGS [10]. Only the viral-mediated integration of the IRF3 optimized human interferon promoter driving the recombinant human IFN-β genes lead to a detectable level of secreted IFN-β (Fig. 4C). Secretion of IFN-β is subsequently associated with the detection of small-induced cytokine CXCL10 in the medium, a clinical marker of IFN-β efficacy. It was thus possible to integrate the acquired data into a model that recapitulates for the synthetic optogenetic pathway dynamics. Pathway activation analysis have also indicated the NIR dependent activation the TLR 3 Axis (Figs. 3,5) linked to the TBK1 activation. These results validate the optogenetic programming strategy to interface cell therapy and optoelectronics into a new generation of implantable bioelectronic medical devices [17].

Animal experiments performed with the EAE mice model confirmed the efficacy of the IFN-β delivery strategy. Despite the signs of progress made in the development of immunotherapies, IFN-β remains an important front-line protein therapeutics to treat multiple sclerosis. As a disease-modifying therapy, its prescription needs to carefully finetune with the disease progression and thus a good candidate for optogenetic cell-based implant delivery. In contrast to a constitutive release mediated by the AVV1-HumIFN-β Adenoviral associated vector, the implantable device offers not only a potential control over the onset of the therapy but also the possibility to remove the device and thus a better safety.

The proof-of-concept preclinical study performed with the EAE mice model illustrates the combined advantages of integrating advanced optoelectronic and optogenetic programming without having to release foreign exogenous genetic material in the patient. Wireless activation of the Optoferon cells confined in the bioelectronic device at the onset of the first manifestation of the EAE symptoms prevented acute demyelination of the animal model (Fig. 8). The positive effects on relapse were comparable to the one observed with the AAV1-IFN-β and a significant preservation of demyelination as well as an improvement of neuroinflammation associated with a reduction of the microglia. Thus, bioelectronic cell-based implants offers an interesting alternative strategy to viral vectors for protein therapeutic delivery.

The design of an implantable medical device encapsulating both cells and optoelectronic imposes strict requirements in the selection and design of the genetic parts as well as the optoelectronic components.

Specific in vitro performance assays were essential for the validation of the selection of the Optogenerapy device industrial manufacturing steps. Experiments conducted with the synthetic optogenetic network components have validated the selection of SMT optoelectronic components compatible with industrial manufacturing pick-and-place assembly lines. A cell chamber assembly process sequentially relying on silicone-based glue was preferred over ultrasonic welding assembly processes to preserve the membrane integrity. Finally, the Optoelectronic coupling performance experiments performed with the Optoferon successfully validated the manufacturing process of the silicon embedded cell chamber devices.

Prototype design iterations using additive manufacturing process helped not only to define the optimal architecture for the injection mold fabrication but also open a new path for the personalization of a future patient-specific implantable device using biocompatible photopolymerizing resins. The wireless power simplifies the architecture of the pre-clinical devices, also a rechargeable battery could be integrated for future application in humans. The development of advanced flexible optoelectronic circuits may offer advantages over classical PCB-based manufacturing. During the prototype's development, both approaches were validated to operate as cell-based drug delivery vehicles. 3D printed manufacturing route integrating PCB optoelectronic offers the flexibility of personalized design associated with the growing source of implantable biocompatible photopolymerizable materials. These options will ease the essential scale-up process to adapt the device architecture to a specific human application. In contrast, the flexible printable optoelectronic (inkjet) advanced manufacturing path supports large batch production and the integration of a programmable optical interface in a cell-based device.

4. Materials and methods

Plasmid production and validation; chemically competent *E.coli* cells (Invitrogen) were used to maintain plasmids. Constructions were synthesized by GenScript gene synthesis services (GenScript) and verified by sanger sequencing (Microsynth). The plasmids were purified using the EndoFree Plasmid Maxi Kit (12362,Qiagen).

Plasmid transfection; HEK293T cells, hMCSc-TERT were transfected with Lipofectamine 3000 reagent in OptiMEM media; ratio: 10 μL Lipofectamine 2000 (Thermofisher) for 4 μg of DNA for 400,000 cells plated a day before transfection.

Production of virus – titer; AAV1-IFN-β (provided by Miguel Esteves) [49] was produced by vectorology platform (iVector core facility). The final titer was 3.61 E13 vg.mL.

Cell culture; HEK 293 T cells (ATCC: CRL-11268) and hMSC-TERT provided by M. Kassem [50], hMSC-MNSOD [51] were maintained in Dulbecco's modified Eagle's medium (DMEM) complemented with 10% fetal bovine serum (FBS), 2 mM L-glutamine, 100 U/mL penicillin, 100 μg/mL streptomycin. Mycozap PR (Lonza). Cells were regularly tested for mycoplasma and viral contamination using the IMPACT screening service (IDEXX bioanalytics).

Determination of hIFN-β concentration; hIFN-β titer were determined by ELISA according to the kit manufacturer's instructions (DuoSet ELISA Human IFN-β kit, R&D Systems.

SEAP assay; 120 μL of substrate solution composed of 100 μL of SEAP assay buffer containing 20 mM homoarginine, 1 mM $MgCl_2$, 21% diethanolamine (pH 9.8), and 20 μL of substrate solution containing 120 mM *p*-nitrophenyl phosphate was added to 80 μL of heat-inactivated (65 °C for 30 min) cell culture supernatant. 405 nm absorbance was measured over time with a plate reader (Infinity; TECAN).

4.1. Quantitative real-time PCR experiments

Cells were grown in 24 well plates and RNA was extracted using the Illustra RNA spin isolation kit (25050071; cytiva lifesciences). cDNA was synthetized using the high-capacity cDNA reverse transcription Kit (4368814; Thermofisher;). Gene expression was quantified with the primer sets described in the supplementary table 1.

Cell-scaffold material; 100 000 cells/well were seeded on cell culture imaging dishes (ibidi plates, Ibidi). Several concentrations; 0; 25; 50 and 100% of the basement membrane matrix scaffolding material (Geltrex LDEV-Free Reduced Growth Factor; A1413201; Thermofisher) were evaluated. Geltrex Extracellular-based matrix concentrations were tested for supporting 3-dimensional growth. The growth of cells was evaluated by microscopic examination at the different focal planes.

The cells were grown in the presence of biliverdin (30891; Sigma-Aldrich) in dark and exposed to NIR light for 4 h. Biliverdin is a present in the blood circulation and does not need to be supplemented in vivo. Microscopic images were taken one and two weeks after the NIR illumination. Cells were imaged in a bright field and to monitor the blue fluorescing marker blueFP.

Loading cells in the device; device loading was described in detail elsewhere [37]. In brief, cells were harvested with 0.05% trypsin-EDTA solution (A3840401; Thermofisher) and resuspended in DMEM/F12 (31331–028; Gibco) culture medium. Two million cells were resuspended in 100 μL DMEM/F12 culture medium. The cell suspension was mixed to 100 μL Geltrex (A1413201; Thermofisher) on ice. An insulin syringe (324826; BD) was used to load devices. The device loading port was sealed with silicon (732; Dow Corning).

NIR activation; in vitro, cells were placed on custom designed 690 nm LED array in a 37 °C.

5% CO_2 incubator.

Device activation; power antenna integrating implant devices were placed in a 6 well culture plate with 2 mL medium 2 cm above a 30 × 15 cm (RD5101 HF, Andrea Electronics) high frequency RFID wireless powering emitter antenna, tuned at 13.56 MHz.

Device manufacturing: the device architecture was drawn with Rhinoceros 3D design software. Device parts were printed using LCD SLA printer and polyJet printer (Stratasys).

Silicon injection molding was performed with a medical grade NUSIL MED-4210 that presents mild curing temperature (around 100 °C).

Flexible optoelectronic; Ink; the first- and third-layer ink are composed of the ELG UV curable conductive silver solids screen printable thick film paste (ELG410S UV; Norcote). The mesh woven with thermotropic liquid crystal polyacrylate thread (V 330–023, V-screen, VECRY) was employed for all the inks. For the flexible screen, Polycarbonate (PC) (Lexan 8010MC 175 μm; Sabic) was selected because it offers high thermal stability and good compatibility for the manufacturing through the injection molding process. The hybridization of SMDs on the plastic foil with printed tracks was performed with a pick-and-place machine (BS281; Autotronik) operating with cure optical medical grade adhesive (MED-OG198–54 UV; EPO-TEK). The stencil technique was fused to deposit the adhesive conductive past to increase the yield of the hybridization process up to 95%. For automation of the process, the circuits were printed in an industrial film cylindrical screen-printing machine (FT-800, ShangHai FengTai Machinery Co.)

Antifibrotic coating; antifibrotic coating of the devices is performed by integrating 25 μg GW2580 (HY-10917; MedChemExpress) crystals in the silicon assembly. GW2580 crystals preparation is described elsewhere [38].

Bioinformatic transcriptomics NGS pathway analysis; transcriptomics profiling using NGS was performed by Eurecat Technology Centre of Catalonia and the analysis conducted with GeneXplain analysis platform (https://genexplain.com/genexplain-platform/). Aligned BAM files were fetched to FeatureCounts tool and generated tables with gene counts were filtered, normalized, and used as Limma input. The lists of significantly up and down regulated genes prepared with limma were used as inputs for the Genome Enhancer pipeline (https://genexplain.com/genome-enhancer/), geneXplain TRANSFAC database is employed together with the TF binding site identification algorithms Match and composite module analyst CMA [34]. The second analysis step involves the signal transduction database TRANSPATH and special graph search algorithms. Target genes were identified from the uploaded experimental data. EdgeR tool (R/Bioconductor package integrated into the pipeline) [52] was applied and compared gene expression with the following sets: “Optoferon NIR 4 h “ with “Optoferon dark 4 h”. EdgeR calculated the LogFC, the *p*-value, and the adjusted p-value (corrected for multiple testing) of the observed fold change. As a result, 2039 genes were found as significantly upregulated (p-value<0.1), and 2373 genes were significantly downregulated (p-value<0.1). Functional analysis of differentially expressed genes was done by mapping the significant up regulated to the ontology of signal transduction and metabolic pathways from the TRANSPATH® database. Statistical significance was computed using a binomial test.

Computational modeling; BioUML platform (http://wiki.biouml.org/index.php/Landing) [53] was used to build the computational model of the genetically engineered pathway. In the model, each variable represents a concentration of the substance of a particular element of the pathway (protein or gene) and the interactions between the elements are modelled with differential equations according to the reaction kinetics. Data describing the mRNA expression and the secretion were integrated with the different node elements describing the synthetic optogenetic pathway (cyclic-di-GMP, STING, TBK1, IRF3, p-IFN ACD+) into a model (Fig. 3). The experimental data were used to fit the model parameters and run a dynamic simulation of the model with an ordinary differential equation (ODE) simulation engine of the BioUML platform.

Animals; Female FVB/NJ and SJL/J mice, Jackson Laboratories (Stock 001800; stock 000686, respectively), were acclimated to the research facility for three weeks before the start of the study. The experiments were carried out following the European Community Council directive (2010/63/EU) for the care and use of laboratory animals.

Four groups of SJL mice aged 6–7 weeks were established: the EAE disease model (EAE; $n = 12$), the EAE disease injected with AVV1-HumIFN-β positive control for treatment (AAV1-IFN-β; $n = 14$); the implant treatment group implanted with the Optogenerapy devices loaded with the Optoferon cells; EAE + implant non activated (OFF, $n = 20$), EAE + activated implant (ON, $n = 22$). In addition, in three SJL mice (WT, $n = 3$) EAE was not induced to allow an analysis of the WT spinal cord.

For the antifibrotic testing: female FVB/NJ mice ($n = 4$) aged 7 months have been implanted for three months with devices coated with antifibrotic compound GW2580.

4.2. Surgery

The surgical procedure was described in detail elsewhere [37]. In brief, mice with a minimum weight of 20 g were used 30 min before induction of anesthesia, meloxicam (5 mg/kg, Boehringer Ingelheim) is maintained three days after surgery. In addition, 10 μL/g of body weight of hydrant saline solution was injected subcutaneously, sterile eye ointment was applied. The surgical procedure was performed under isoflurane (IsoVet, 1000 mg/kg, Vetflurane, Virbac). Induction of anesthesia was 4% isoflurane. Anesthetized mice were kept on a 37 °C heating blanket. The skin on the surgical site was shaved and disinfected with chlorhexidine 0.05% (5% Hibitane). An incision of 1 cm was performed in dorsal skin and subcutaneous skin of the back was cleared from muscle creating a surgical window. The subcutaneous tissue was spread with blunt-ended forceps to create a pocket for the implant. The device was placed subcutaneously. Subcutaneous tissue was sutured using resorbable suture (PGLA07CN; Vicryl 6.0; Vetsuture) and the incision with non-resorbable suture polypropylene (LENE1CN; Vetsuture). Animals were maintained at 37 °C during the postoperative recovery. Daily monitoring of weight and wound healing was performed.

Immunization of EAE model mouse; Two weeks after the implantation of the bioelectronic implant device, EAE induction was performed in all SJL mice aged nine weeks. PLP139–151/CFA (CFA (EK-2120; Hooke Kit; Hookelabs) was injected subcutaneously, 50 μL both in the upper and lower back. Then an injection of pertussis was performed in intraperitoneal (0.1 mL/animal) (PLP139–151/CFA Emulsion PTX EK-2120; Hooke Kit).

EAE neurological score; A neurological score was performed in all mice every day. The standard scoring system was used, whereby 0 = no paralysis, 1 = loss of tail tone, 1 = for each limb paralysis, and 6 = moribund. An “in-between” score (i.e., 0.5, 1.5, 2.5, 3.5) was retained when the clinical picture lies between two defined scores.

Wireless device activation; at the onset of the first EAE symptoms, devices of mice of group EAE + Implant ON were activated by placing the mice colony housing on the wireless powering RF antenna twice per week for 6 h. As treatment control, EAE + AVV1-HumIFN-β mice were retro-orbitally injected with an adenoviral vector (1.6 10e11 vg).

The sacrifice of animals; SJL mice and 129OLA B6J mice were sacrificed with a lethal dose of Euthasol (180 mg.Kg, Vetcare) 26 days after immunization or four months after implantation. Animals' cadavers were perfused with PBS. Skin, liver, spleen, and spinal cord were collected and post-fixated with PFA 4% overnight. The skin of female 129OLA B6J mice was collected and post-fixated with PFA 4% overnight. Samples were dehydrated in alcohol to be included in paraffin. Samples were sliced at 4 or 6 μm with a microtome (RM2245 Leica).

Viability of cells; trypan blue staining was used in routine to evaluate cell viability. For the explanted device, cells were collected from the device in 1.5 mL reaction tube. Recovered cells were diluted (1:4) in sterile PBS and loaded with a cytofunnel (A78710003EZ, cytofunnel Shandon, Thermofisher) to a Shandon single cytoslide (Thermofisher, 5991059). Cells were fixed with PFA 4% for 15 min. After two PBS

washing, cells were stained in DAPI, and cells viability assessed with trypan blue dye exclusion test.

In vitro scratch assay; the assay was performed to assess the cell migration of the engineered cells. Confluent cells were scratch with a pipette tips to give a uniform gap in-between cells, cell migration is observed after 8 h.

Fluorescence imaging in vivo; in vivo 3D quantitative near-infrared fluorescence diffuse optical tomography (fDOT) equipped with two lasers (680 nm and 740 nm) was used to monitor the implantation of the device loaded HEK-NirFP two weeks post-implantation in animals. Rodent transdermal NIR fluorescence emission was monitored under anesthesia.

Histological staining, hematoxylin-eosin staining; Liver, spleen, and skin were stained with hematoxylin-eosin. Briefly, after dewaxed and rehydrated sections, samples were stained with Mayer's hematoxylin (C0303, DiaPath) for 3 min and counter-stained with eosin. The dehydrated sections mounted with Eukitt® (VWR) were acquired using a slide scanner (Axioscan, Zeiss) and quantified using the ZEN software (Zeiss).

Quantification of demyelination with Luxol staining; spinal cord myelin sections were stained with Luxol (L0294, Sigma**).** Slices were acquired using digital slide scanner (Hamamatsu Photonics). Slides were analyzed using FIJI software (ImageJ). Measurement of the total area of myelin was integrated on the lumbar spinal cord using Fiji software and normalized by the total spinal cord area and done by a blind experimentator in view of the group. The myelin percentage was reported as 100% in WT and results are reported compared to WT untreated animals.

Immunostaining; Microgliosis were analyzed by immunostaining with rabbit anti-Iba1 (1:500 dilution; G-3893; Sigma-Aldrich). The immunohistochemical labeling was performed using the Avidin-Biotin Complex (ABC method). Briefly, after treatment with 0.9% H2O2/0.3% Triton/PBS for 30 min followed of PBS washes, sections were treated with citrate 10 mM pH 6 at 110 °C for 5 min (Decloaking ChamberTM NxGen, Biocare Medical), PBS washed and incubated with the blocking solution (10% goat serum in PBS/0.3% TritonX-100) for 1 h. The primary antibodies were diluted in blocking solution and incubated on tissue sections overnight at 4 °C. After washes in PBS, sections were sequentially incubated with goat anti-mouse or goat anti-rabbit antibodies conjugated to biotin (Vector Laboratories), followed by the avidin-biotin complex staining kit (Vector Laboratories). Peroxidase activity was detected using diaminobenzidine as chromogen (Dako, Carpinteria, CA). In some cases, the slides were counterstained with hematoxylin. The slides were mounted with Eukitt (VWR International). Slices were acquired using a slide scanner used at 20 X (Axioscan, Zeiss).

Tools to analyze the biocompatibility of devices; a score assessing the device biocompatibility was applied for three days in post-surgery integrating tissue inflammation, reopening of the wound, scratching. Details of the scoring are described elsewhere [37]. Different parameters of the tissue at the implantation site were quantified. The thickness of the epidermis and the muscle were measured in 5–6 areas of the skin section for each animal. The area of adipose tissue was measured in a minimum of 50 areas for each animal. The neovascularization of the devices was evaluated by hematoxylin eosin staining and confirmed by von Willebrand factor staining. The number of blood vessels was counted at the implantation in 6 areas of the skin section for each animal. The diameter of blood vessels measured in 6 areas of the skin section for each animal. A repartition of blood vessel size was performed for each animal. The muscle degeneracy was assessed in 6 areas of the skin section for each animal. The number of nuclei bearing muscle fibers was enumerated for each area. A mean of each parameter by area was performed for each animal [37].

4.3. Statistical analysis

Data were quantified using GraphPad Prism 8 software. The statistical significance of values among groups was evaluated by analysis of variance (ANOVA), followed by the least significant difference *t*-test. All values used in figures and text are expressed as mean ± standard error of the mean (SEM). The difference was considered significant when the *P*-value was 0.05 or less.

Author contributions

MFo, FP, NC, CD, EE, PB Conceptualization. EA, FM, VP, TK, LR, BG, GD, MFl, AB, MF, KA and FP Investigation and data curation. MFo, FP, CD, EE, NC, AK Supervision. MFo, EA, FP, EE, CDWriting review and editing.

Declaration of Competing Interest

The authors declare no conflicts of interest.

Data availability

Data will be made available on request.

Acknowledgement

Funding source: This project has received funding from the European Union's Horizon 2020 research and innovation program under grant agreement No. 720694. Part of this work was carried out in the iVector Core facility, Histomics core facility, CELIS cell culture core facility and PHENOPARC core facility of ICM. We thank Clémence Tournaire for technical assistance.

Appendix A. Supplementary data

Supplementary data to this article can be found online at https://doi.org/10.1016/j.jconrel.2022.11.008.

References

[1] R.M.T. Ten Ham, J. Hoekman, A.M. Hovels, A.W. Broekmans, H.G.M. Leufkens, O. H. Klungel, Challenges in advanced therapy medicinal product development: a survey among companies in Europe, Mol Ther Methods Clin Dev 11 (2018) 121–130.

[2] L. Scheller, M. Fussenegger, From synthetic biology to human therapy: engineered mammalian cells, Curr. Opin. Biotechnol. 58 (2019) 108–116.

[3] A.D. Agulnick, D.M. Ambruzs, M.A. Moorman, A. Bhoumik, R.M. Cesario, J. K. Payne, J.R. Kelly, C. Haakmeester, R. Srijemac, A.Z. Wilson, J. Kerr, M. A. Frazier, E.J. Kroon, K.A. D'Amour, Insulin-producing endocrine cells differentiated in vitro from human embryonic stem cells function in macroencapsulation devices in vivo, Stem Cells Transl. Med. 4 (2015) 1214–1222.

[4] K. Krawczyk, S. Xue, P. Buchmann, G. Charpin-El-Hamri, P. Saxena, M.D. Hussherr, J. Shao, H. Ye, M. Xie, M. Fussenegger, Electrogenetic cellular insulin release for real-time glycemic control in type 1 diabetic mice, Science 368 (2020) 993–1001.

[5] M. Farina, J.F. Alexander, U. Thekkedath, M. Ferrari, A. Grattoni, Cell encapsulation: overcoming barriers in cell transplantation in diabetes and beyond, Adv. Drug Deliv. Rev. 139 (2019) 92–115.

[6] P. Saxena, G. Charpin-El Hamri, M. Folcher, H. Zulewski, M. Fussenegger, Synthetic gene network restoring endogenous pituitary-thyroid feedback control in experimental Graves' disease, Proc. Natl. Acad. Sci. U. S. A. 113 (2016) 1244–1249.

[7] A.P. Teixeira, M. Fussenegger, Synthetic biology-inspired therapies for metabolic diseases, Curr. Opin. Biotechnol. 47 (2017) 59–66.

[8] M.H. Ryu, O.V. Moskvin, J. Siltberg-Liberles, M. Gomelsky, Natural and engineered photoactivated nucleotidyl cyclases for optogenetic applications, J. Biol. Chem. 285 (2010) 41501–41508.

[9] M. Folcher, Photoactivatable Nucleotide Cyclases for Synthetic Photobiology Applications, Cambridge University Press, in: Cambridge, 2017 pp. pp 118-131.

[10] M. Folcher, S. Oesterle, K. Zwicky, T. Thekkottil, J. Heymoz, M. Hohmann, M. Christen, M. Daoud El-Baba, P. Buchmann, M. Fussenegger, Mind-controlled transgene expression by a wireless-powered optogenetic designer cell implant, Nat. Commun. 5 (2014) 5392.

[11] J. Shao, S. Xue, G. Yu, Y. Yu, X. Yang, Y. Bai, S. Zhu, L. Yang, J. Yin, Y. Wang, S. Liao, S. Guo, M. Xie, M. Fussenegger, H. Ye, Smartphone-controlled optogenetically engineered cells enable semiautomatic glucose homeostasis in diabetic mice, Sci. Transl. Med. 9 (2017).

[12] A. Lathuiliere, S. Cosson, M.P. Lutolf, B.L. Schneider, P. Aebischer, A high-capacity cell macroencapsulation system supporting the long-term survival of genetically engineered allogeneic cells, Biomaterials 35 (2014) 779–791.

[13] A. Lathuiliere, V. Laversenne, A. Astolfo, E. Kopetzki, H. Jacobsen, M. Stampanoni, B. Bohrmann, B.L. Schneider, P. Aebischer, A subcutaneous cellular implant for passive immunization against amyloid-beta reduces brain amyloid and tau pathologies, Brain 139 (2016) 1587–1604.

[14] O.M. Sabek, M. Farina, D.W. Fraga, S. Afshar, A. Ballerini, C.S. Filgueira, U. R. Thekkedath, A. Grattoni, A.O. Gaber, Three-dimensional printed polymeric system to encapsulate human mesenchymal stem cells differentiated into islet-like insulin-producing aggregates for diabetes treatment, J Tissue Eng 7 (2016), 2041731416638198.

[15] M. Salmi, Additive manufacturing processes in medical applications, Materials (Basel) 14 (2021).

[16] Q. Yan, H.H. Dong, J. Su, J.H. Han, B. Song, Q.S. Wei, Y.S. Shi, A review of 3D printing technology for medical applications, Engineering-Prc 4 (2018) 729–742.

[17] M. Michel, M. Folcher, Optogenerapy: when bio-electronic implant enters the modern syringe era, Porto Biomed. J. 2 (2017) 145–149.

[18] Y.F. Luo, M. Wang, C.J. Wan, P.Q. Cai, X.J. Loh, X.D. Chen, Devising materials manufacturing toward lab-to-fab translation of flexible electronics, Adv. Mater. 32 (2020).

[19] I.F. Hung, K.C. Lung, E.Y. Tso, R. Liu, T.W. Chung, M.Y. Chu, Y.Y. Ng, J. Lo, J. Chan, A.R. Tam, H.P. Shum, V. Chan, A.K. Wu, K.M. Sin, W.S. Leung, W.L. Law, D.C. Lung, S. Sin, P. Yeung, C.C. Yip, R.R. Zhang, A.Y. Fung, E.Y. Yan, K.H. Leung, J.D. Ip, A.W. Chu, W.M. Chan, A.C. Ng, R. Lee, K. Fung, A. Yeung, T.C. Wu, J. W. Chan, W.W. Yan, W.M. Chan, J.F. Chan, A.K. Lie, O.T. Tsang, V.C. Cheng, T. L. Que, C.S. Lau, K.H. Chan, K.K. To, K.Y. Yuen, Triple combination of interferon beta-1b, lopinavir-ritonavir, and ribavirin in the treatment of patients admitted to hospital with COVID-19: an open-label, randomised, phase 2 trial, Lancet 395 (2020) 1695–1704.

[20] E. Bosi, C. Bosi, P. Rovere Querini, N. Mancini, G. Calori, A. Ruggeri, C. Canzonieri, L. Callegaro, M. Clementi, F. De Cobelli, M. Filippi, M. Bregni, Interferon beta-1a (IFNbeta-1a) in COVID-19 patients (INTERCOP): study protocol for a randomized controlled trial, Trials 21 (2020) 939.

[21] PRISMS (Prevention of Relapses and Disability by Interferon beta-1a Subcutaneously in Multiple Sclerosis) Study Group, Randomised double-blind placebo-controlled study of interferon beta-1a in relapsing/remitting multiple sclerosis, Lancet 352 (1998) 1498–1504.

[22] M. Marziniak, S. Meuth, Current perspectives on interferon Beta-1b for the treatment of multiple sclerosis, Adv. Ther. 31 (2014) 915–931.

[23] C.H. Goldschmidt, L.H. Hua, Re-evaluating the use of IFN-beta and relapsing multiple sclerosis: safety, efficacy and place in therapy, Degener Neurol Neuromuscul Dis 10 (2020) 29–38.

[24] L.A. Visser, M. Folcher, C. Delgado Simao, B. Gutierrez Arechederra, E. Escudero, C.A. Uyl-de Groot, W.K. Redekop, The potential cost-effectiveness of a cell-based bioelectronic implantable device delivering interferon beta 1a therapy versus injectable interferon beta 1a treatment in relapsing-remitting multiple sclerosis, PharmacoEconomics. 40 (1) (2022) 91–108.

[25] A. Hamana, Y. Takahashi, A. Tanioka, M. Nishikawa, Y. Takakura, Amelioration of experimental autoimmune encephalomyelitis in mice by interferon-Beta gene therapy, using a long-term expression plasmid vector, Mol. Pharm. 14 (2017) 1212–1217.

[26] K.P. Hopfner, V. Hornung, Molecular mechanisms and cellular functions of cGAS-STING signalling, Nat. Rev. Mol. Cell Biol. 21 (2020) 501–521.

[27] C.R. Escalante, E. Nistal-Villan, L. Shen, A. Garcia-Sastre, A.K. Aggarwal, Structure of IRF-3 bound to the PRDIII-I regulatory element of the human interferon-beta enhancer, Mol. Cell 26 (2007) 703–716.

[28] N.A. Twine, L. Harkness, J. Adjaye, A. Aldahmash, M.R. Wilkins, M. Kassem, Molecular phenotyping of Telomerized human bone marrow skeletal stem cells reveals a genetic program of enhanced proliferation and maintenance of differentiation responses, JBMR Plus 2 (2018) 257–267.

[29] M.H. Ryu, M. Gomelsky, Near-infrared light responsive synthetic c-di-GMP module for optogenetic applications, ACS Synth. Biol. 3 (2014) 802–810.

[30] U. Koppe, K. Hogner, J.M. Doehn, H.C. Muller, M. Witzenrath, B. Gutbier, S. Bauer, T. Pribyl, S. Hammerschmidt, J. Lohmeyer, N. Suttorp, S. Herold, B. Opitz, Streptococcus pneumoniae stimulates a STING- and IFN regulatory factor 3-dependent type I IFN production in macrophages, which regulates RANTES production in macrophages, cocultured alveolar epithelial cells, and mouse lungs, J. Immunol. 188 (2012) 811–817.

[31] R. Vazirinejad, Z. Ahmadi, M. Kazemi Arababadi, G. Hassanshahi, D. Kennedy, The biological functions, structure and sources of CXCL10 and its outstanding part in the pathophysiology of multiple sclerosis, Neuroimmunomodulation 21 (2014) 322–330.

[32] M. Buttmann, C. Merzyn, P. Rieckmann, Interferon-beta induces transient systemic IP-10/CXCL10 chemokine release in patients with multiple sclerosis, J. Neuroimmunol. 156 (2004) 195–203.

[33] P. Malik, N. Zuleger, J.I. de las Heras, N. Saiz-Ros, A.A. Makarov, V. Lazou, P. Meinke, M. Waterfall, D.A. Kelly, E.C. Schirmer, NET23/STING promotes chromatin compaction from the nuclear envelope, PLoS One 9 (2014), e111851.

[34] A.E. Kel, Search for master regulators in walking Cancer pathways, Methods Mol. Biol. 1613 (2017) 161–191.

[35] T. Waleev, D. Shtokalo, T. Konovalova, N. Voss, E. Cheremushkin, P. Stegmaier, O. Kel-Margoulis, E. Wingender, A. Kel, Composite module analyst: identification of transcription factor binding site combinations using genetic algorithm, Nucleic Acids Res. 34 (2006) W541–W545.

[36] U. Boyarskikh, S. Pintus, N. Mandrik, D. Stelmashenko, I. Kiselev, I. Evshin, R. Sharipov, P. Stegmaier, F. Kolpakov, M. Filipenko, A. Kel, Computational master-regulator search reveals mTOR and PI3K pathways responsible for low sensitivity of NCI-H292 and A427 lung cancer cell lines to cytotoxic action of p53 activator Nutlin-3, BMC Med. Genet. 11 (2018) 12.

[37] E. Audouard, L. Rousselot, M. Folcher, N. Cartier, F. Piguet, Optimized protocol for subcutaneous implantation of encapsulated cells device and evaluation of biocompatibility, Front. Bioeng. Biotechnol. 9 (2021).

[38] S. Farah, J.C. Doloff, P. Muller, A. Sadraei, H.J. Han, K. Olafson, K. Vyas, H.H. Tam, J. Hollister-Lock, P.S. Kowalski, M. Griffin, A. Meng, M. McAvoy, A.C. Graham, J. McGarrigle, J. Oberholzer, G.C. Weir, D.L. Greiner, R. Langer, D.G. Anderson, Long-term implant fibrosis prevention in rodents and non-human primates using crystallized drug formulations, Nat. Mater. 18 (2019) 892–904.

[39] Y.N. Gerber, G.P. Saint-Martin, C.M. Bringuier, S. Bartolami, C. Goze-Bac, H. N. Noristani, F.E. Perrin, CSF1R inhibition reduces microglia proliferation, promotes tissue preservation and improves motor recovery after spinal cord injury, Front. Cell. Neurosci. 12 (2018) 368.

[40] J. He, H. Hsuchou, Y. He, A.J. Kastin, P.K. Mishra, J. Fang, W. Pan, Leukocyte infiltration across the blood-spinal cord barrier is modulated by sleep fragmentation in mice with experimental autoimmune encephalomyelitis, Fluids Barriers CNS 11 (2014) 27.

[41] F. Fallegger, G. Schiavone, S.P. Lacour, Conformable hybrid Systems for Implantable Bioelectronic Interfaces, Adv. Mater. 32 (2020).

[42] T.B. Lopez-Mendez, E. Santos-Vizcaino, J.L. Pedraz, R.M. Hernandez, G. Orive, Cell microencapsulation technologies for sustained drug delivery: clinical trials and companies, Drug Discov. Today 26 (3) (2020) 852–861.

[43] W. Tao, Application of encapsulated cell technology for retinal degenerative diseases, Expert. Opin. Biol. Ther. 6 (2006) 717–726.

[44] R.R. Henry, J. Pettus, J. Wilensky, A.M.J. Shapiro, P.A. Senior, B. Roep, R. Wang, E. J. Kroon, M. Scott, K. D'Amour, H.L. Foyt, Initial clinical evaluation of VC-01TM combination product-a stem cell-derived islet replacement for type 1 diabetes (T1D), Diabetes 67 (2018).

[45] A. Rezania, J.E. Bruin, P. Arora, A. Rubin, I. Batushansky, A. Asadi, S. O'Dwyer, N. Quiskamp, M. Mojibian, T. Albrecht, Y.H. Yang, J.D. Johnson, T.J. Kieffer, Reversal of diabetes with insulin-producing cells derived in vitro from human pluripotent stem cells, Nat. Biotechnol. 32 (2014) 1121–1133.

[46] F. Schwenter, S. Zarei, P. Luy, V. Padrun, N. Bouche, J.S. Lee, R.C. Mulligan, P. Morel, N. Mach, Cell encapsulation technology as a novel strategy for human anti-tumor immunotherapy, Cancer Gene Ther. 18 (2011) 553–562.

[47] C. Weber, S. Pohl, R. Portner, C. Wallrapp, M. Kassem, P. Geigle, P. Czermak, Cultivation and differentiation of encapsulated hMSC-TERT in a disposable small-scale syringe-like fixed bed reactor, Open Biomed Eng J 1 (2007) 64–70.

[48] S. Valadkhan, L.M. Plasek, Long non-coding RNA-mediated regulation of the interferon response: a new perspective on a familiar theme, Pathog Immun 3 (2018) 126–148.

[49] H. Petry, L. Cashion, P. Szymanski, O. Ast, A. Orme, C. Gross, M. Bauzon, A. Brooks, C. Schaefer, H. Gibson, H. Qian, G.M. Rubanyi, R.N. Harkins, Mx1 and IP-10: biomarkers to measure IFN-beta activity in mice following gene-based delivery, J. Interf. Cytokine Res. 26 (2006) 699–705.

[50] J.L. Simonsen, C. Rosada, N. Serakinci, J. Justesen, K. Stenderup, S.I. Rattan, T. G. Jensen, M. Kassem, Telomerase expression extends the proliferative life-span and maintains the osteogenic potential of human bone marrow stromal cells, Nat. Biotechnol. 20 (2002) 592–596.

[51] P. Bourgine, C. Le Magnen, S. Pigeot, J. Geurts, A. Scherberich, I. Martin, Combination of immortalization and inducible death strategies to generate a human mesenchymal stromal cell line with controlled survival, Stem Cell Res. 12 (2014) 584–598.

[52] M.D. Robinson, D.J. McCarthy, G.K. Smyth, edgeR: a Bioconductor package for differential expression analysis of digital gene expression data, Bioinformatics 26 (2010) 139–140.

[53] F. Kolpakov, I. Akberdin, I. Kiselev, S. Kolmykov, Y. Kondrakhin, M. Kulyashov, E. Kutumova, S. Pintus, A. Ryabova, R. Sharipov, I. Yevshin, S. Zhatchenko, A. Kel, BioUML-towards a universal research platform, Nucleic Acids Res. 50 (W1) (2022) w124–w131.